Universidade de São Paulo

Biblioteca Digital da Produção Intelectual - BDPI

Departamento de Física e Ciências Materiais - IFSC/FCM Artigos e Materiais de Revistas Científicas - IFSC/FCM

2012

Electronic structure, growth mechanism and photoluminescence of CaW'O IND. 4' crystals

CrystEngComm,Cambridge : Royal Society of Chemistry - RSC,v. 14, n. 3, p. 853-868, 2012
http://www.producao.usp.br/handle/BDPI/49535

Downloaded from: Biblioteca Digital da Produção Intelectual - BDPI, Universidade de São Paulo

View Online / Journal Homepage / Table of Contents for this issue
Dynamic Article Links

CrystEngComm

Cite this: *CrystEngComm*, 2012, **14**, 853

www.rsc.org/crystengcomm

PAPER

Electronic structure, growth mechanism and photoluminescence of $CaWO_4$ crystals†

L. S. Cavalcante,*[a] V. M. Longo,[a] J. C. Sczancoski,[a] M. A. P. Almeida,[b] A. A. Batista,[b] J. A. Varela,[a] M. O. Orlandi,[a] E. Longo[a] and M. Siu Li[c]

Received 1st August 2011, Accepted 5th October 2011
DOI: 10.1039/c1ce05977g

Published on 18 November 2011 on http://pubs.rsc.org | doi:10.1039/C1CE05977G
Downloaded by UNIVERSIDAD SAO PAULO on 07 February 2012

In this paper, aggregated $CaWO_4$ micro- and nanocrystals were synthesized by the co-precipitation method and processed under microwave-assisted hydrothermal/solvothermal conditions (160 °C for 30 min). According to the X-ray patterns, all crystals exhibited only the scheelite-type tetragonal structure. The data obtained by the Rietveld refinements revealed that the oxygen atoms occupy different positions in the $[WO_4]$ clusters, suggesting the presence of lattice distortions. The crystal shapes as well as its crystallographic orientations were identified by field-emission scanning electron microscopy and high-resolution transmission electron microcopy. Electronic structures of these crystals were evaluated by the first-principles quantum mechanical calculations based on the density functional theory in the B3LYP level. A good correlation was found between the experimental and theoretical Raman and infrared-active modes. A crystal growth mechanism was proposed to explain the morphological evolution. The ultraviolet-visible absorption spectra indicated the existence of intermediary energy levels within the band gap. The highest blue photoluminescence emission, lifetime and quantum yield were observed for the nanocrystals processed in the microwave-assisted solvothermal method.

Introduction

In recent years, molybdates and tungstates belonging to the scheelite-type tetragonal structure[1–4] have been extensively investigated by the scientific community for technological applications in acousto-optic filters,[5] solid state lasers[6,7] light-emitting diodes,[8] photocatalysts,[9,10] phosphors,[11–13] scintillators,[14–16] microwave dielectrics,[17,18] and cryogenic scintillation detectors.[19,20] Among these materials, the pure or rare earth-doped calcium tungstate ($CaWO_4$) has been studied because of its photoluminescence (PL) emissions in the visible wavelength regions of the electromagnetic spectrum.[21–24] For example, Zhang *et al.*[25] analyzed the temperature-dependent PL behavior of $CaWO_4$ microspheres synthesized by the surfactant-assisted solution route. According to these authors, there is a reduction in the blue emission intensities with the temperature evolution. The absence of green light emission bands at liquid-nitrogen temperatures was related to the non-existence of defect centers. Phuruangrat *et al.*[26] and Thongtem *et al.*[27] concluded that the violet-blue PL emissions of $CaWO_4$ arise from $^1T_2 \rightarrow {}^1A_2$ electronic transitions within the $[WO_4]^{2-}$ groups. Orhan *et al.*[28] explained that the PL properties of $CaWO_4$ thin films are sensitive to the degree of structural order–disorder. However, despite several theories and hypotheses published on the PL properties, the key factors responsible for its origin or modification in the $CaWO_4$ crystals are not yet completely explained. Hence, the corroboration between experimental and theoretical results can be a powerful tool to understand the nature of this optical phenomenon.

In general, tungstates with the scheelite-type tetragonal structure (space group ($I4_1/a$)) are characterized by an arrangement of $[WO_4]$ (tetrahedral coordination) and $[AO_8$; A = Ca, Sr, Ba, Pb] (deltahedral coordination) clusters.[29–32] In this structure, there are strong bonds between the [···O–W–O···] with its neighbouring [···A–O–A···] clusters, whose internal/external vibration spectra provide information on the structure and degree of order–disorder in the lattice.[33,34] The symmetry breaking in these clusters can arise from different factors, such as: distortions on the $[WO_4]$ clusters, modifications on the O–W–O bond lengths, changes on the dihedral angles, and formation of oxygen vacancies. It is well-established that the effects of structural order–disorder occur at short, medium or long-range.[33] Therefore, these kinds of structural defects modify the electronic band structure of tungstates, affecting its PL properties.[34,35] In a previous work reported by our research group,[36] it was shown that the crystal shapes, particle size distribution and crystallographic orientations were able to change the PL behaviour of $CaMoO_4$ crystals.

[a]*Universidade Estadual Paulista, P.O. Box 355, CEP. 14801-907 Araraquara, SP, Brazil. E-mail: laeciosc@bol.com.br*
[b]*Universidade Federal de São Carlos, P.O. Box 676, CEP. 13565-905, São Carlos, SP, Brazil*
[c]*IFSC-Universidade de São Paulo, P.O. Box 369, 13560-970 São Carlos, SP, Brazil*
† Electronic supplementary information (ESI) available. See DOI: 10.1039/c1ce05977g

View Online

Published on 18 November 2011 on http://pubs.rsc.org | doi:10.1039/C1CE05977G
Downloaded by UNIVERSIDAD SAO PAULO on 07 February 2012

Currently, it is well-established in the literature that the chemical and physical properties of inorganic solids are extremely dependent on the structure, composition, purity, crystallographic phase, size and size distribution.[37–39] Hence, the field of materials science has a scientific interest in the development of new chemical strategies and/or synthetic techniques with the ability to control or manipulate the particle shapes and sizes (nano-, meso- or micro-scale), employing low temperatures and short synthesis times.[36] In this viewpoint, the hydrothermal systems can be considered excellent candidates for these purposes. In particular, Komarneni *et al.*[40–42] solved the problems of thermal gradients as well as the slow reaction kinetics of conventional hydrothermal (CH) equipment, implementing microwave radiation as an energy source. The improvement in this experimental apparatus, known as microwave-hydrothermal (MH), was able to minimize the processing times (few minutes or some hours) and increase the level of crystallization of the particles. These advantages of MH in relation to CH arise from the direct interaction of the microwaves with the ions or molecules in solution and/or with the solid phases dispersed in the liquid medium. In fact, it is important to highlight that the efficiency in the conversion capacity of microwave energy into thermal energy is governed by the physics variables: loss tangent, relaxation time and penetration depth.[43] For these reasons and also to avoid or minimize the agglomeration process between the particles, the non-aqueous solvents (glycerol, ethylene glycol, propylene glycol) have been frequently used in microwave-assisted synthesis.[44,45]

Therefore, in this paper, aggregated $CaWO_4$ micro- and nanocrystals were synthesized by the co-precipitation (CP) method and processed in the MH and microwave-solvothermal (MS) systems at 160 °C for 30 min. The structural characterizations were performed by X-ray diffraction (XRD), Rietveld refinements, Fourier transform Raman (FT-Raman) and Fourier transform infrared (FT-IR) spectroscopies. The crystal shapes and sizes were investigated by means of field-emission scanning electron microscopy (FE-SEM), and transmission electron microcopy (TEM). The optical properties were focused on the ultraviolet-visible (UV-vis) absorption spectra and PL measurements. The electronic band structure and density of states of $CaWO_4$ micro- and nanocrystals were theoretically calculated in order to understand the effect of structural distortions on the PL profiles. The theoretical models were appropriate to represent the different degree of structural order–disorder in the lattice.

Experimental details

Synthesis and MH/MS processing of $CaWO_4$ crystals

The typical experimental procedure is described as follows: 1×10^{-3} mol of tungstate sodium dihydrate ($Na_2WO_4 \cdot 2H_2O$) (99% purity, Aldrich) and 1×10^{-3} mol of calcium acetate monohydrated [$Ca(CH_3COO)_2 \cdot H_2O$] (99% purity, Aldrich) were dissolved in 100 mL of deionized water (H_2O) under constant stirring at 80 °C for 1 h. Afterwards a non aqueous solution with the tungsten and calcium precursors were dissolved in 100 mL of propane-1,2-diol [$C_3H_8O_2$] (99.5% purity, DOW) at 130 °C for 6 h. In principle, during the co-precipitation (CP) reaction, the Ca^{2+} cations (Lewis acid–electron-pair acceptor) interact with the WO_4^{2-} anions (Lewis base–electron-pair donor), resulting in the formation of $CaWO_4$ precipitates (eqn (1), (2)).

$$Na_2WO_4 \cdot 2H_2O + Ca(CH_3COO)_2 \cdot H_2O \xrightarrow{H_2O(80\ ^\circ C/1\ h)} CaWO_4 + 2Na^+ + 2CH_3CO_2^- + 3H_2O \quad (1)$$

$$Na_2WO_4 \cdot 2H_2O + Ca(CH_3COO)_2 \cdot H_2O \xrightarrow{C_3H_8O_2(130\ ^\circ C/6\ h)} CaWO_4 + 2Na^+ + 2CH_3CO_2^- + 3H_2O \quad (2)$$

Afterwards, the colloidal suspensions containing the precipitates were transferred to a Teflon autoclave, which was sealed and placed inside an adapted microwave oven (2.45 GHz, 800 W).[46] The MH and MS processing were performed at 160 °C for 30 min (eqn (3), (4)).

$$CaWO_4 \xrightarrow[\approx Microwaves \approx]{H_2O(160\ ^\circ C/30\ min)} CaWO_4 \quad (3)$$

$$CaWO_4 \xrightarrow[\approx Microwaves \approx]{C_3H_8O_2(160\ ^\circ C/30\ min)} CaWO_4 \quad (4)$$

In both cases, the heating rate was fixed at 25 °C min^{-1} and the pressure inside the autoclave stabilized at 1 atm ($C_3H_8O_2$ – solvothermal condition) and 5 atm (H_2O – hydrothermal condition), respectively. Then the autoclaves were naturally cooled to room temperature. These suspensions were centrifuged and washed several times with deionized water and acetone to remove the Na^+ ions and/or organic residual solvents. Finally, the white precipitates were collected and dried in a hot plate at 70 °C for 6 h.

Characterizations of the $CaWO_4$ crystals

The aggregated $CaWO_4$ micro- and nanocrystals were structurally characterized using a D/Max-2500PC diffractometer (Rigaku, Japan) with Cu-Kα radiation ($\lambda = 1.5406$ Å) in the 2θ range from 5° to 75° with scanning rate of 0.02° min^{-1} (exposure time of 15 min). The Rietveld routines were performed in the 2θ range from 10° to 110° with scanning rate of 0.02° min^{-1} (exposure time of 90 min). The FT-Raman spectroscopies were recorded in the range from 50 cm^{-1} to 1,000 cm^{-1} with a RFS100 spectrophotometer (Bruker, Germany). The spectra were obtained using a Nd:YAG laser ($\lambda = 1064$ nm), keeping its maximum output power at 100 mW. The viscosities of the solvents were estimated at room temperature using a rheometer (Brookfield DV-III Ultra, USA). The FT-IR spectroscopies were carried out in the range from 200 cm^{-1} to 1,000 cm^{-1} with a MB-102 spectrophotometer (Bomem-Michelson, Switzerland) in transmittance mode. In these measurements, small quantities of $CaWO_4$ were mixed with potassium bromide powder and then compressed into thin transparent pellets using a hydraulic press. The morphologies were investigated through a Supra 35-VP FEG-SEM (Carl Zeiss, Germany) operated at 6 kV and with a CM200 transmission electron microscope (Philips, Netherlands) operated at 200 kV. In the sample preparation for the TEM technique, the obtained powders were firstly dispersed in ethanol using an ultrasonic bath for 20 min. Afterwards, the suspensions were deposited on the copper grids *via* fast immersion. The UV-vis spectra were taken using a Cary 5G spectrophotometer (Varian, USA) in diffuse

 This journal is © The Royal Society of Chemistry 2012

Published on 18 November 2011 on http://pubs.rsc.org | doi:10.1039/C1CE05977G
Downloaded by UNIVERSIDAD SAO PAULO on 07 February 2012

reflection mode. The PL measurements were performed with a Monospec 27 monochromator (Thermal Jarrel Ash, USA) coupled to a R446 photomultiplier (Hamamatsu Photonics, Japan). A krypton ion laser (Coherent Innova 90 K, USA) ($\lambda = 350$ nm) was used as excitation source, keeping its maximum output power at 500 mW. After passing through the optical chopper, the maximum laser power was reduced and kept at 40 mW on the samples. An optical parametric oscillator was employed for lifetime measurements. All experimental measurements were performed at room temperature.

Computational method and periodic model of $CaWO_4$ crystals

The simulation was performed using a periodic approximation as implemented in the CRYSTAL06 computer code.[47] The computational method is based on the density functional theory in conjunction with Becke's three parameter hybrid nonlocal exchange functional,[48] combined with the Lee–Yang–Parr gradient-corrected correlation functional, B3LYP.[49] Hybrid density-functional methods have been extensively used for molecules, providing an accurate description of crystalline structures, bond lengths, binding energies, and band-gap values.[50] The diagonalization of the Fock matrix was performed at adequate *k*-point grids (Pack–Monkhorst 1976) in the reciprocal space.[51] The thresholds controlling the accuracy of the calculation of Coulomb and exchange integrals were set to 10^{-8} (ITOL1 to ITOL4) and 10^{-14} (ITOL5), whereas the percent of Fock/Kohn–Sham matrices mixing was set to 30 (IPMIX = 30).[51] The dynamical matrix was computed by numerical evaluation of the first-derivative of the analytical atomic gradients. The point group symmetry of the system was fully exploited to reduce the number of points to be considered. On each numerical step, the residual symmetry was preserved during the self-consistent field method (SCF) and the gradients calculation. The atomic centers have been described by the basis sets for the Ca and W atoms were used the 86-511d21G and PS-11d3G pseudopotential basis sets, respectively, provided by the CRYSTAL basis sets library, and oxygen atoms have been described by the standard 6-31G*.[52a] *k*-point sampling was chosen as 36 points within the irreducible part of the Brillouin zone. The XcrysDen program was used to design the diagrams of the band structure.[52b] The analysis of the vibrational modes and its corresponding frequencies were calculated through numerical second derivatives of the total energies as implemented in the CRYSTAL06 package.[47] Based on the theoretical and experimental results, three models were constructed, a theoretical derived from optimized structure and two structures, that were not optimized, derived from Rietveld refinement data to better describe the structural distortions derived from the experimental synthesis.

Results and discussion

X-Ray diffraction analyses

Fig. 1 shows the XRD patterns of aggregated $CaWO_4$ micro- and nanocrystals processed in MH and MS conditions.

All diffraction peaks were perfectly indexed to the scheelite-type tetragonal structure with space group $I4_1/a$ (Inorganic Crystal Structure Database (ICSD) No. 18135).[53] Secondary phases were not observed in the diffractograms, revealing that

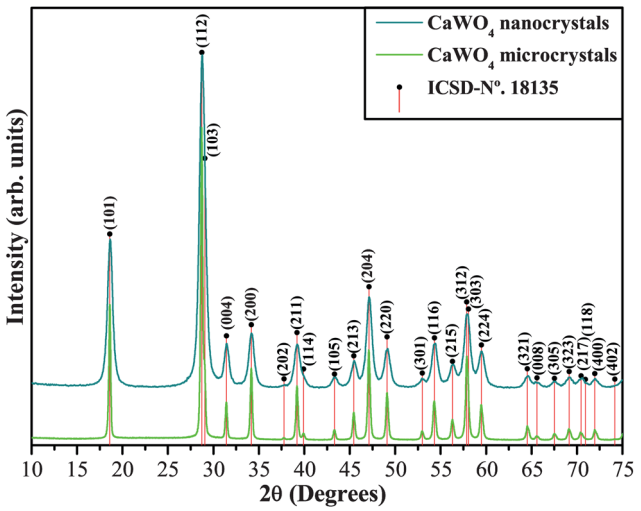

Fig. 1 XRD patterns of aggregated $CaWO_4$ micro- and nanocrystals processed in MH and MS, respectively.

the MH and MS processing were not able to promote the phase segregation, but only the crystal growth. In addition, the presence of strong and sharp diffraction peaks is a typical characteristic of materials structurally ordered at long-range.[54] The slightly broadening in the peaks was most evident for the $CaWO_4$ processed in MS, *i.e.*, a common phenomenon found in solid systems composed of nanoparticles.[55] The experimental lattice parameters and unit cell volumes were calculated using the Rietveld refinement method[56] with the Maud program (version 2.26).[57,58] These obtained data are shown in Table 1 (Support information Fig. SI-1†).

In this case, it was noted that the lattice parameters and unit cell volumes are very close to those published in the literature.[59–62] The small variations between these values can be related to the peculiarity of each synthesis method, where the experimental variables (temperature, time processing, heating rate, solvents *etc.*) are able to influence the organization of the [CaO_8] and [WO_4] clusters within the scheelite structure. These variables can cause the formation or reduction of structural defects (oxygen vacancies, distortion on the bonds, stresses and strains on the crystalline lattice) in the materials. In previous work, we reported on the presence of residual stresses and/or distortions in strontium and barium tungstates.[63,64a] According to Li *et al.*,[64b] a decrease in the *c*/*a* axis ratio is expected since the dipole–dipole interactions on the polar and surfaces (001) might have a very limited influence on the lattice dimension, which explains the enhanced structural symmetry in $CaWO_4$ nanocrystals. As a result, the variability of axis length along *c* and *a* directions is reasonable to occur, owing to the different arrangements and reduction in *c*/*a* that promotes more distortion on the tetrahedra WO_4 clusters in $CaWO_4$ nanocrystals. Therefore, the results obtained in our work are in good agreement with the literature.[64b]

Rietveld refinements data analyses

Fig. 2(a,b) illustrate the structural refinements of aggregated $CaWO_4$ micro- and nanocrystals processed in MH and MS, respectively.

Table 1 Comparative results between the lattice parameters and unit cell volume of $CaWO_4$ micro- and nanocrystals obtained in this work with those published in the literature.[a]

M	T (° C)	t (min)	Lattice $a = b$	Parameters c/Å	b/c ratio	c/a ratio	V (Å^3)	Ref.
FG	1350	120	5.243	11.376	0.46088	2.1697	312.715	59
SSR	900	120	5.238	11.374	0.461	2.1689	312.064	60
CZ	1200	240	5.2055	11.2757	0.46165	2.1661	305.54	61
HC	160	720	—	—	—	—	311.827	62
MH	160	30	5.2434(2)	11.3794(3)	0.46078	2.1702	312.85	[Ħ]
MS	160	30	5.247(1)	11.3834(2)	0.46093	2.1695	313.39	[Ħ]
THEO	—	—	5.2019(4)	11.2961(4)	0.4605	2.1715	305.68	[Ħ]
ICSD	N°. 18135	—	5.2425(5)	11.3715(5)	0.4610	2.1690	312.53	53

[a] M = method, T = temperature; t = processing time; a, b, c = Lattice parameters, V = Unit cell volume, $\alpha = \beta = \gamma$ angles = 90°, Ref. = references, FG = flux growth; SSR = solid-state reaction; CZ = Czochralski, HC = hydrothermal conventional, MH = microwave-hydrothermal, MS = microwave-solvothermal, THEO = Theoretical and [Ħ] = this work.

Published on 18 November 2011 on http://pubs.rsc.org | doi:10.1039/C1CE05977G
Downloaded by UNIVERSIDAD SAO PAULO on 07 February 2012

The Rietveld refinement method[56] was employed to understand whether there are differences in the structural arrangements of $CaWO_4$ micro- and nanocrystals processed in MH and MS. The refinement technique is based on the least-squares approach, where the theoretical peak profiles[65] are adjusted up to converge with the measured profiles. The Rietveld refinement presents several advantages on the conventional quantitative analysis methods,[66] including: use of pattern-fitting algorithms and all lines of each crystallographic phase are explicitly considered (even those overlapped lines). Thus, it is not necessary to decompose the patterns into separate Bragg peaks. The use of all reflections in a pattern, rather than just the strongest ones, minimizes the uncertainty in the derived weight fractions and the effects of preferred orientation, primary extinction, and nonlinear detection systems.[67] Also, the structural refinements can be optimized using the Rietveld texture and stress analyses.[68] According to the literature,[69,70] the various data arising from structural refinements are generally checked by the quality algorithms or R-factors (R_{wnb}, R_b, R_{exp}, R_w and σ). However, the difference between the measured and calculated patterns is considered a way to verify the success of the refinement.

In our work, the optimized parameters were scale factor, background with exponential shift, exponential thermal shift and polynomial coefficients, basic phase, microstructure, crystal structure, size-strain (anisotropic no rules), structure solution model (genetic algorithm SDPD), shift lattice constants, profile half-width parameters (u, v, w), texture, lattice parameters (a, b, c), factor occupancy, atomic site occupancies (Wyckoff).[70–72] In the Rietveld refinements, the measured diffraction patterns were well-adjusted to the Crystallographic Information File (CIF) No. 18135.[53] The generated CIF files for each $CaWO_4$ nanocrystal are displayed in the Supporting information – Table-SI-1.† In fact, the results arising from structural refinements are commonly acceptable under the following criteria: (a) $R_w < 10\%$ – medium complex phases (tetragonal, orthorhombic, rhombohedral and hexagonal); (b) $R_w < 15\%$ – high complex phases (monoclinic and triclinic); (c) $R_w < 8\%$ – cubic structure (high symmetry and few diffraction peaks).[68] Also, the low σ values (< 2) are indicative of good accuracy for the obtained refinement results. As can be observed in Fig. 2(a,b), the good fit between the experimental and calculated XRD patterns proves the accuracy of the structural refinements performed on the $CaWO_4$ micro- and nanocrystals. These results from Rietveld refinements are displayed in Table 2.

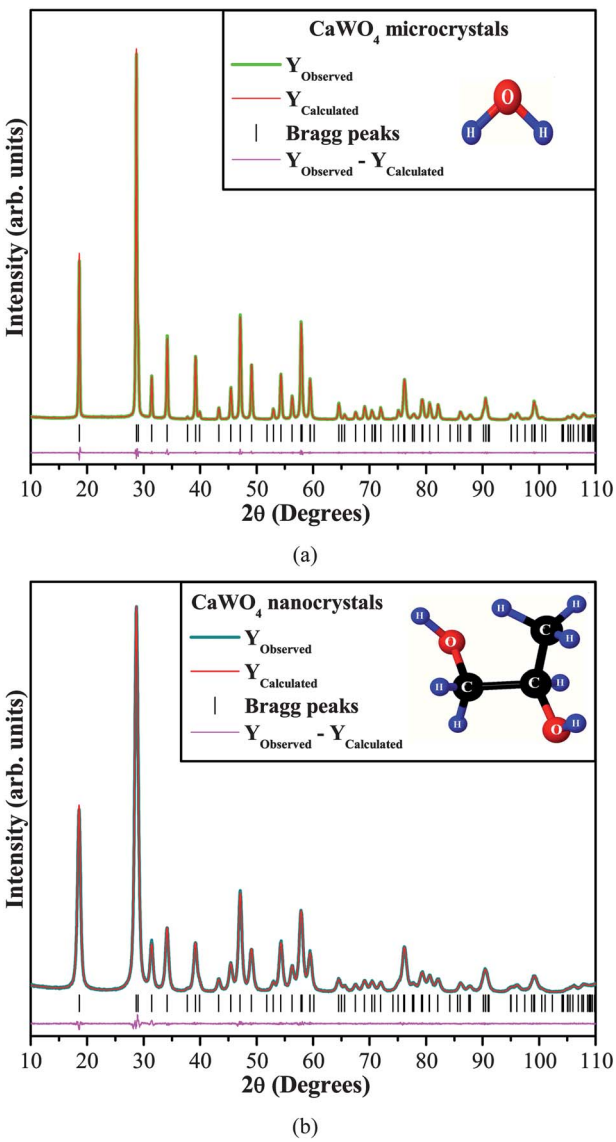

Fig. 2 Rietveld refinements of aggregated $CaWO_4$ (a) micro- and (b) nanocrystals processed in MH and MS, respectively.

This journal is © The Royal Society of Chemistry 2012

Published on 18 November 2011 on http://pubs.rsc.org | doi:10.1039/C1CE05977G
Downloaded by UNIVERSIDAD SAO PAULO on 07 February 2012

In this table, the fit parameters (R_{wnb}, R_b, R_{exp}, R_w and σ) suggest that the refinement results are very reliable. It is interesting to note that there are considerable variations in the atomic positions related to the oxygen atoms, while the calcium and tungsten atoms keep fixed their positions within the structure. These results indicate the existence of structural distortions on the [CaO_8] and [WO_4] clusters of $CaWO_4$ nano- and microcrystals, which can be induced by the different levels of coupling between the microwave radiation with the solvents (H_2O, $C_3H_8O_2$). The lattice parameters and internal coordination estimated from the optimized structure (theoretical model) and refined parameters are listed in Tables 1 and 2, respectively.

Unit cell representations of $CaWO_4$ crystals

Fig. 3(a,b) show the representations of two $CaWO_4$ unit cells.

The lattice parameters and atomic positions obtained by means of Rietveld refinements (Tables 1 and 2) were used in the Diamond Crystal and Molecular Structure Visualization program (Version 3.2f for Windows)[73] to model these unit cells (space group $I4_1/a$ and point-group symmetry C_{4h}^6).[74] In both unit cells, the tungsten (W) atoms are coordinated to four oxygens, forming the tetrahedral [WO_4] clusters (4 vertices, 4 faces and 6 edges).[75] Moreover, as it can be seen in Fig. 3(a,b), there are changes in the O–W–O bond angles, revealing that the [WO_4] clusters are slightly distorted within the lattice. In principle, it arises from the experimental preparation conditions for the formation and crystallization of $CaWO_4$ phase, such as: co-precipitation rate, interaction of microwave radiation with the solvents (H_2O or $C_3H_8O_2$) and/or dispersed solid phases in this medium. It was noted that the nanocrystals (Fig. 3(b)) exhibited more distorted clusters than the microcrystals (Fig. 3(a)).

In terms of organization of calcium atoms within the scheelite, they are coordinated to eight oxygens ([CaO_8] clusters), adopting a snub disphenoide polyhedron (8 vertices, 12 faces and 18 edges) with deltahedral coordination and point-group symmetry D_{2d}).[76] These clusters also present dihedral angle distortions, however, it is more complex than the detected for those of [WO_4]. More details on this phenomena are presented in the Supporting Information – Fig. SI-2(a,b).†

Table 2 Comparison between the atomic coordinates obtained by the Rietveld refinements of $CaWO_4$ micro- and nanocrystals with those reported in the CIF file No. 18135.[a]

♣ Atoms	Wyckoff	Site	*x*	*y*	*z*
Calcium	4*b*	−4	0	0.25	0.625
Tungsten	4*a*	−4	0	0.25	0.125
Oxygen	16*f*	1	0.1497	0.0093	0.2097
$R_w = 3.8\%$; $R_{wnb} = 3.1\%$; $R_b = 2.7\%$; $R_{exp} = 3.3\%$ and $\sigma = 1.15$					
♠ Atoms	**Wyckoff**	**Site**	***x***	***y***	***z***
Calcium	4*b*	−4	0	0.25	0.625
Tungsten	4*a*	−4	0	0.25	0.125
Oxygen	16*f*	1	0.25096	0.10003	0.04763
$R_w = 3.4\%$; $R_{wnb} = 2.9\%$; $R_b = 2.3\%$; $R_{exp} = 2.8\%$ and $\sigma = 1.21$					
★ Atoms	**Wyckoff**	**Site**	***x***	***y***	***z***
Calcium	4*b*	−4	−0.5	−0.5	0.125
Tungsten	4*a*	−4	0	0.25	0.125
Oxygen	16*f*	1	0.2399	0.10149	0.040514

[a] ♣ = $CaWO_4$ microcrystals (MH), ♠ = $CaWO_4$ nanocrystals (MS), and ★ = Theoretical.

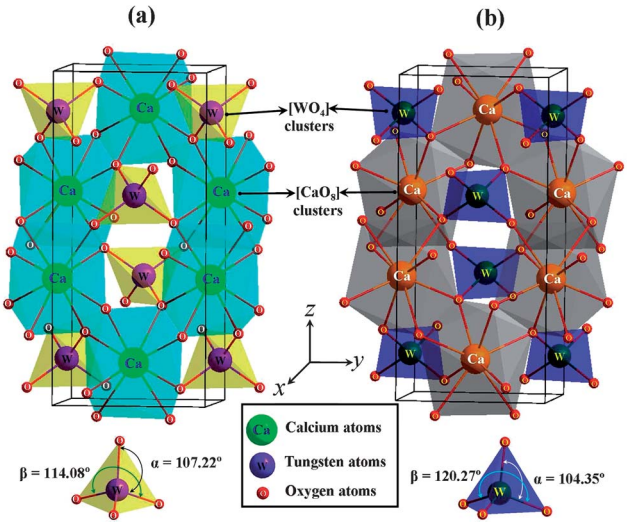

Fig. 3 Schematic representation of the unit cells corresponding to the aggregated $CaWO_4$ (a) micro- and (b) nanocrystals processed in MH and MS, respectively.

Fourier-transform Raman/infrared spectroscopies: Theoretical and experimental analyses

The group theory shows that the $CaWO_4$ crystals have 26 distinct vibration modes (Raman and infrared), as indicated in eqn (5):[77,78]

$$\Gamma_{(Raman\ +\ Infrared)} = 3A_g + 5A_u + 5B_g + 3B_u + 5E_g + 5E_u \quad (5)$$

where the A_g, B_g, and E_g are Raman-active modes. The A and B modes are nondegenerate, while the E modes are doubly degenerate. The subscripts "g and u" indicate the parity under inversion in centrosymmetric $CaWO_4$ crystals. The A_u and E_u modes correspond to the zero frequency of acoustic modes, while the others are optic modes. In addition, the A_g, B_g, and E_g modes arise from the same motion in a $CaWO_4$ phase. Thus, 13 zone-center Raman-active modes for the $CaWO_4$ crystals are expected, as described in eqn (6):[79,80]

$$\Gamma_{(Raman)} = 3A_g + 5B_g + 5E_g \quad (6)$$

According to the literature,[81,82] the vibrational modes detected in the Raman spectra of tungstates can be classified into two groups, external and internal modes. The vibration external modes are related to the lattice phonon or motion of [CaO_8] clusters. The vibrational internal modes are caused by the vibration of [WO_4] clusters, considering the center of mass in stationary state. An isolated [WO_4] cluster has cubic symmetry point (T_d)[83] and its vibrations are composed of four modes ($\nu_1(A_1)$, $\nu_2(E_1)$, $\nu_3(F_2)$) and $\nu_4(F_2)$), one free rotation mode $\nu_{f.r.}$ (F_1) and one translation mode (F_2). On the other hand, when the [WO_4] clusters are located into the scheelite structure, its point symmetry is reduced to S_4.[70] In vibrational infrared spectra, $1A_u$

Published on 18 November 2011 on http://pubs.rsc.org | doi:10.1039/C1CE05977G
Downloaded by UNIVERSIDAD SAO PAULO on 07 February 2012

and $1E_u$ acoustic are infrared-inactive mode and $3B_u$ forbidden infrared modes. Therefore, only 8 infrared-active vibration modes remain, as presented by eqn (7):[83,84]

$$\Gamma_{(\text{Infrared})} = 4A_u + 4E_u, \quad (7)$$

Fig. 4(a,b) illustrate the FT-Raman spectra and specific theoretical/experimental Raman shifts of $CaWO_4$ crystals, respectively.

As it can be observed in Fig. 4(a), the spectra revealed the presence of eleven Raman-active vibration modes. Two modes (one A_g and one E_g) were not detectable because of their low intensities. The literature[86,87] reports that the Raman spectroscopy can be employed as a probe to investigate the degree of structural order–disorder at short-range in the materials. Based on this concept, the Raman spectrum consisting of sharp, intense and well-defined vibration bands is commonly verified in solids with local structural order. This phenomenon was identified in both aggregated $CaWO_4$ micro- and nanocrystals processed in the MH and MS systems (Fig. 4(a)). The theoretical Raman-active modes were calculated through the atomic positions and lattice parameters for the optimized $CaWO_4$ phase. The relative positions of these vibration modes are illustrated in Fig. 4(b) and presented in Table 3.

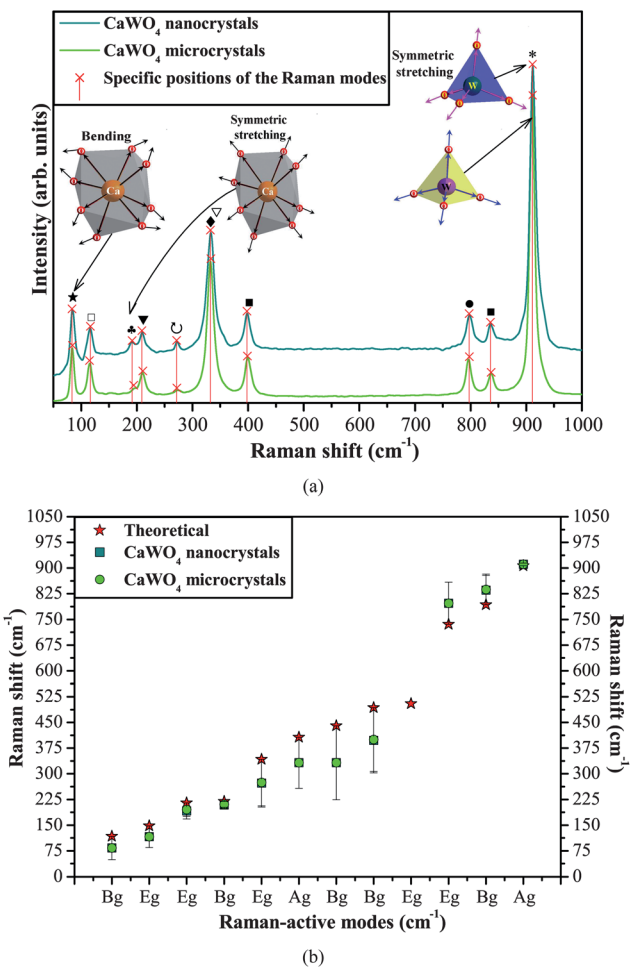

Fig. 4 (a) FT-Raman spectra of aggregated $CaWO_4$ (a) micro- and (b) nanocrystals processed in MH and MS, illustrating the stretching and bending modes of $[WO_4]$ and $[CaO_8]$ clusters; (b) comparative between the relative positions of theoretical and experimental Raman-active modes.

There is a good agreement between the Raman-active modes of $CaWO_4$ nanocrystals with those previously published[81,82,85,88] (Table 3). These results were proved by means of theoretical calculations, however, the E_g mode (505 cm^{-1}) was not experimentally identified (Fig. 4(b)). Thus, it is possible to conclude that this mode has the lowest intensity in the spectrum. In addition, when also compared to the literature, the slight variations in the typical positions of the vibration modes can be caused by the preparation methods, average crystal size, distortions on the (O–W–O)/(O–Ca–O) bonds, interaction forces involving the $[WO_4]$–$[CaO_8]$–$[WO_4]$ clusters and/or different degrees of order–disorder structural within the lattice.

Fig. 5(a,b) illustrate the FT-IR spectra and corresponding theoretical/experimental positions of IR-active modes of $CaWO_4$ crystals, respectively.

As was previously discussed in the text, the tungstates with scheelite-type structure have eight stretching and/or bending IR-active vibrational modes.[89,90] In our case, no more than six modes [$2A_u$, $1(A_u + E_u)$ and $3E_u$] were identified in the spectra (Fig. 5(a)). Firstly, the $CaWO_4$ nanocrystals exhibited an overlapping of two intense absorption bands ($\nu_3(1E_u$ and $1A_u)$ in the range from 794 cm^{-1} to 862 cm^{-1}, which were ascribed to the $(\leftarrow O \leftarrow W \leftarrow O\leftarrow)/(\rightarrow O \rightarrow W \rightarrow O\rightarrow)$ anti-symmetric stretching vibrations within the $[WO_4]$ clusters (Fig. 5(a)). The $\nu_4[1(A_u + E_u)]$ modes situated at around 438 cm^{-1} arise from symmetric bending vibrations within the $[WO_4]$ clusters.[91] The $\nu_2(A_u)$ internal mode found at 323 cm^{-1}/333 cm^{-1} is due to the symmetric bending vibrations within the $[WO_4]$ clusters. Finally, the other two $R_{x,y}$ $(1E_u)$ and $L_{x,y}$ $(1E_u)$ external modes at around 276 and 220 cm^{-1} are related to the torsional motion of $[WO_4]$ clusters and translation of $[CaO_8]$ clusters, respectively. The typical theoretical and experimental positions IR-actives modes are shown in Fig. 5(b) and listed in Table 4.

Fig. 5(b) indicated a good conformity between the wavenumbers of the experimental and calculated infrared-active modes. In addition, the theoretical results showed the evidence of two $(2A_u)$ modes at 209 cm^{-1} and 529 cm^{-1}, which were not experimentally detected because of the low detection limit imposed by the FT-IR spectrophotometer. In terms of spectral positions, the small deviations in the IR-active modes of $CaWO_4$ nano- and microcrystals can be attributed to the different degrees of interaction and modification on the O–W–O bond lengths and/or angles within the $[WO_4]$ clusters. Moreover, the results reported in this work are very close to those published in the literature.[84,92–94]

FE-SEM analyses and average size distribution of $CaWO_4$ crystals

Fig. 6(a–g) show the FE-SEM images and average size distribution of $CaWO_4$ crystals processed in MH and MS systems at 160 °C for 30 min.

FE-SEM image in Fig. 6(a) showed the presence of several irregular spherical-like $CaWO_4$ microcrystals with agglomerate nature, and polydisperse particle size distribution (Fig. 6(a)).

 This journal is © The Royal Society of Chemistry 2012

Table 3 Comparative results between the experimental and theoretical Raman-active modes of $CaWO_4$ micro- and nanocrystals obtained in this work with those published in the literature.[a]

M	T (° C)	t (min)	B_g ★	E_g □	E_g ♣	B_g ▼	E_g ○	A_g ◆	B_g ∇	B_g ■	E_g •	B_g ■	A_g *	Ref.
IC	—	—	86	117	195	218	275	336	336	401	797	838	912	81
CZ	1200	2400	86	117	195	217	274	337	337	400	797	839	911	82
CH	190	24	—	—	—	210	—	332	332	398	799	839	915	85
CZ	1100	1440	84	116	196	212	276	334	334	402	797	838	911	88
MS	160	30	84	116	192	209	273	332	332	398	797	836	911	[Ħ]
MH	160	30	84	116	196	211	275	332	332	400	797	838	911	[Ħ]
THEO	—	—	118	148	215	219	343	407	440	493	736	793	907	[Ħ]

[a] M = method; T = temperature; t = time; Raman modes = (cm^{-1}); IC = Isomet corporation, CZ = Czochralski; CH = Conventional hydrothermal; MH = Microwave-hydrothermal, MS = Microwave-solvothermal, THEO = Theoretical and [Ħ] = this work.

Downloaded by UNIVERSIDAD SAO PAULO on 07 February 2012
Published on 18 November 2011 on http://pubs.rsc.org | doi:10.1039/C1CE05977G

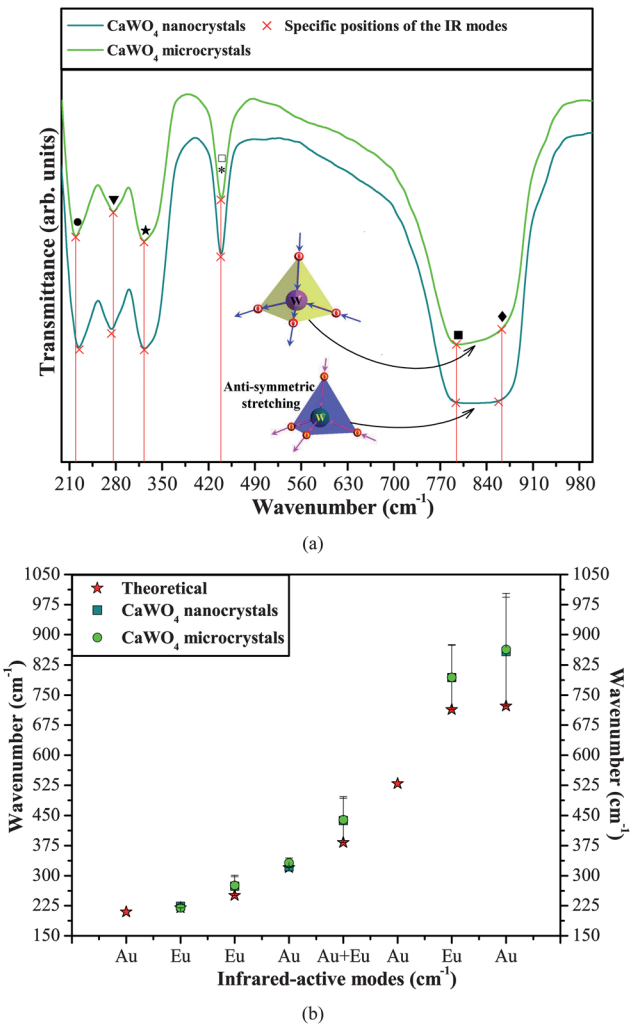

Fig. 5 (a) FT-IR spectra of aggregated $CaWO_4$ micro- and nanocrystals processed in MH and MS. Insets show the anti-symmetric stretching vibrations of [WO_4] clusters; (b) comparative between the relative positions of theoretical and experimental IR-active modes.

These images suggest that after the precipitation process occurred a fast formation, growth and agglomeration of small crystals. These $CaWO_4$ microcrystals can be clearly identified in the high magnification FE-SEM images, like in Fig. 6(b). As can be noted in the inset of Fig. 6(b), these small crystals spontaneously aggregated into complex superstructures. It is important to emphasize that the FE-SEM images were also employed to evaluate the average crystal size distribution by means of the counting of 100 crystals (presenting a good surface contour to ensure the authenticity of the statistical response). The irregular spherical-like $CaWO_4$ microcrystals processed in aqueous medium exhibited an average size distribution in the range from 0.75 μm to 4.75 μm (Fig. 6(c) and inset). In this system, it was estimated that 28% of these superstructures have an average size of approximately 2.75 μm. On the other hand, the counting of small $CaWO_4$ crystals by the TEM and HR-TEM images indicated an average particle size distribution from 10 nm to 210 nm (Fig. 6(d) and inset). Fig. 6(e,f) revealed the presence of several aggregated $CaWO_4$ nanocrystals formed in $C_3E_8O_2$, where the single nanocrystals have an irregular octahedron shape (dotted white rectangle in Fig. 6(f)). Therefore, it is possible to deduce that several crystallites nucleated and grew into small seed particles. These octahedron-like nanocrystals exhibited an average size distribution in the range from 5 nm to 25 nm (Fig. 6 (g)). In principle, this reduction in the crystal sizes was induced by the high viscosity (53.6 mPa.s) and adsorption of $C_3H_8O_2$ on the $CaWO_4$ surfaces (Fig. 6(g) and inset).

Table 4 Comparative results between the experimental and theoretical IR-active modes of $CaWO_4$ micro- and nanocrystals obtained in this work with those published in the literature.[a]

M	T (° C)	t (min)	E_u •	E_u ▼	A_u ★	$E_u + A_u$ * □	E_u ■	A_u ◆	Ref.
CZ	1100	1440	204	252	327	366	—	796	84
CP	30	1440	—	—	—	461	657	966	92
CZ	1100	1440	204	252	327	366	—	796	93
PSG	800	120	—	—	—	442	—	830	94
MS	160	30	224	274	322	438	794	858	[Ħ]
MH	160	30	219	276	322	439	794	863	[Ħ]
THEO	—	—	220	251	320	383	714	723	[Ħ]

[a] M = method; T = temperature; t = time; Infrared modes = (cm^{-1}); CZ = Czochralski; CP = co-precipitation, PSG = Pechini sol–gel; MS = Microwave-solvothermal, MH = Microwave-hydrothermal, THEO = Theoretical and [Ħ] = this work.

TEM analyses of $CaWO_4$ crystals

Fig. 7(a–f) show the TEM images and selected area electron diffraction (SAED) patterns of $CaWO_4$ crystals processed in MH and MS systems at 160 °C for 30 min.

Published on 18 November 2011 on http://pubs.rsc.org | doi:10.1039/C1CE05977G
Downloaded by UNIVERSIDAD SAO PAULO on 07 February 2012

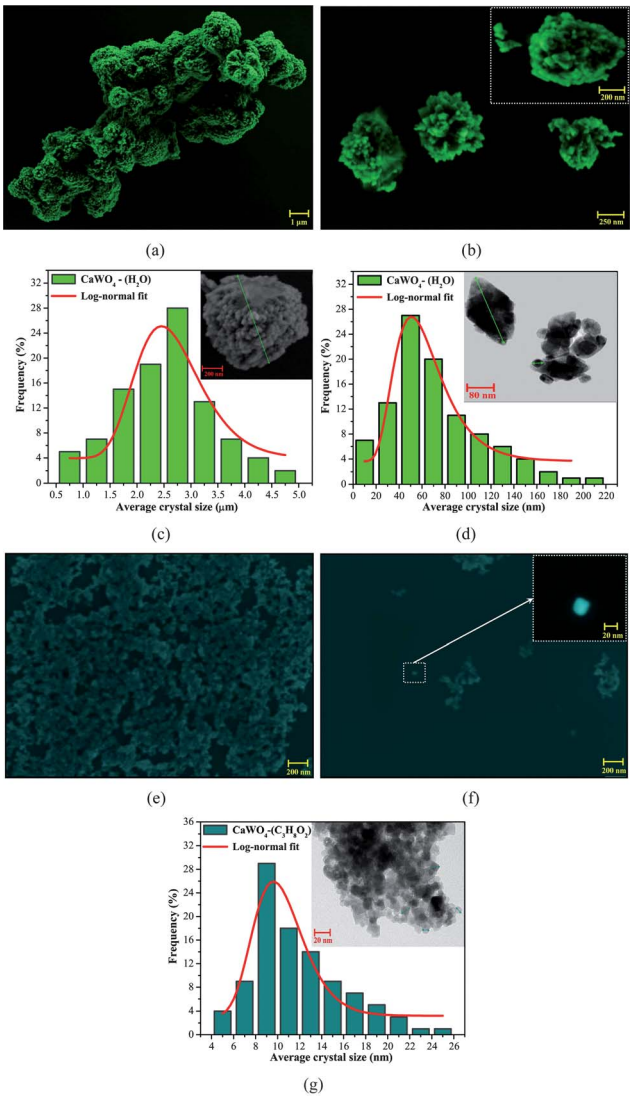

Fig. 6 (a,b) Low and high magnification FE-SEM images of aggregated $CaWO_4$ microcrystals obtained in MH, respectively. Inset in (b) shows an individual $CaWO_4$ microcrystal (dotted yellow square); (c) average size distribution of aggregated microcrystals; (d) average particle size distribution of individual crystals; (e,f) low and high magnification FE-SEM images of aggregated $CaWO_4$ nanocrystals formed in MS, respectively. Inset in (f) illustrates an individual $CaWO_4$ nanocrystal (dotted white rectangle); (g) average size distribution of aggregated nanocrystals.

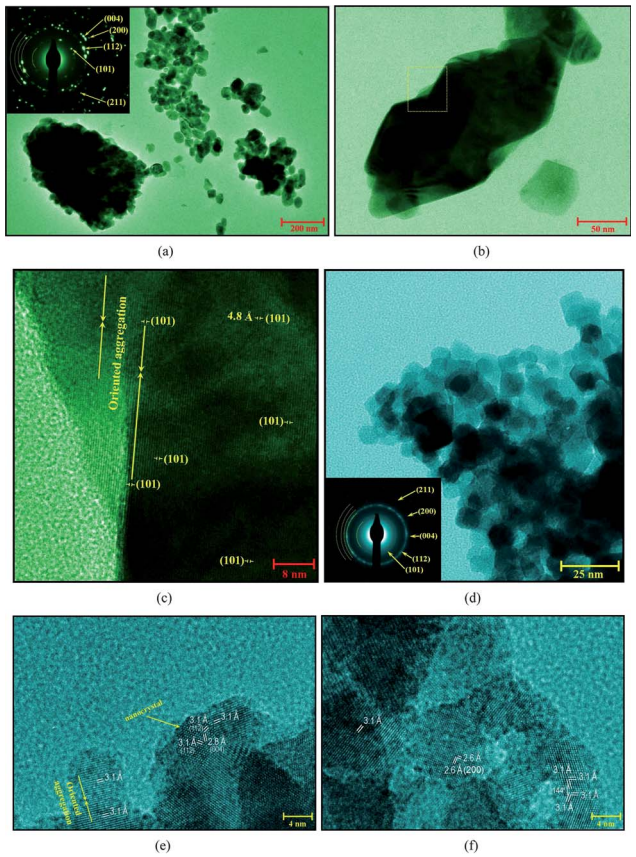

Fig. 7 (a) Low magnification TEM image of aggregated $CaWO_4$ microcrystals obtained in MH. Inset shows its corresponding SAED patterns; (b) HR-TEM image of small octahedron-like $CaWO_4$ crystals; (c) HR-TEM image performed between two crystals in (b) (dotted yellow square); (d) low magnification TEM image of aggregated $CaWO_4$ nanocrystals formed in MS. Inset shows its corresponding SAED patterns; (e,f) HR-TEM images of several $CaWO_4$ nanocrystals, where some of them are randomly aggregated and others are oriented in similar crystallographic orientations.

Fig. 7(a) illustrates the low magnification TEM image of irregular spherical-like $CaWO_4$ microcrystals obtained only in H_2O (100 mL) under MH conditions (160 °C for 30 min). In this micrograph, the dark areas are related to the high concentration of aggregated crystals, confirming also that these structures are not internally hollow.[95] The SAED performed on the nanocrystals and spherical-like $CaWO_4$ microcrystals presented common electron diffraction patterns of polycrystalline materials, as a consequence of the aggregated nature (Inset in Fig. 7 (a)). However, high resolution (HR-TEM) images demonstrated that there are some small crystals oriented on the same (112) crystallographic plane (Supporting Information – Fig. 3(a,b)†). In Fig. 7(b), the low magnification TEM image suggests the existence of oriented aggregation in a small ensemble of octahedron-like crystals. A typical example of this phenomenon can be evidenced in Fig. 7(c), where the chosen region (dotted yellow square) revealed the occurrence of attachments between two nanocrystals along the (101) plane (planar spacing of 4.8 Å). A large quantity of aggregated $CaWO_4$ nanocrystals were identified in the TEM images in Fig. 7(d). In this system prepared only with $C_3H_8O_2$, the different crystallographic orientations of the nanocrystals resulted in an electron diffraction ring pattern by the SAED technique (Inset in Fig. 7(d)). In principle, this behavior found for the $CaWO_4$ nanocrystals obtained under MS treatment is caused by the adsorption of solvent molecules (with polymer characteristic) on the crystal faces, inhibiting the growth anisotropy in specific directions.[96] In addition, it was chosen by some nanocrystals in different regions (Supporting Information – Fig. SI-3(c,d)†). From the HR-TEM images in Fig. 7(e), the oriented aggregation phenomenon was also verified in some nanocrystals attached in the (112) plane (crystallographic distance of approximately 3.1 Å). In this figure, there is also a random stacking of nanocrystals containing distinct

 This journal is © The Royal Society of Chemistry 2012

View Online

crystallographic orientations ((112) and (004) planes). Besides the spontaneous aggregation process, in some circumstances imperfect oriented attachment occurred causing the formation of angles between nanocrystals with a common crystallographic in the (112) plane (Fig. 7(f)). In fact, the growth and mutual aggregation of $CaWO_4$ nanocrystals processed in the MS system can be related to the $C_3H_8O_2$ solvent, where it is able to minimize the diffusion velocity of (Ca^{2+}) to $(WO)_4^{2-}$ ions because of its high viscosity as well as influence the collision and interaction between two adjacent nanocrystals.[97]

Growth mechanism of $CaWO_4$ crystals

Fig. 8(a–f) illustrate a schematic representation of all stages involved during the synthesis and growth of $CaWO_4$ crystals processed in the MH and MS systems.

Fig. 8(a) shows the synthesis procedure adopted for the preparation of $CaWO_4$ crystals. Firstly, stoichiometric quantities of $Ca(CH_3COO)_2{\cdot}H_2O$ and $Na_2WO_4{\cdot}2H_2O$ precursors were separately dissolved in two tubes containing 50 mL of deionized water. In this solution, the solvation energy of H_2O molecules causes a fast dissociation of the reagents, *i.e.*, the Ca^{2+} and WO_4^{2-} ions are quickly solvated by the H_2O molecules. The partial negative charges of these molecules are electrostatically attracted by the Ca^{2+} ions, while its positive charges attract the WO_4^{2-} ions. Due to the difference of electronic density of both Ca^{2+} and WO_4^{2-} ions, occurs a strong electrostatic attraction between them. An important point to be considered is the fact that the solvents (H_2O and $C_3H_8O_2$) have distinct possibilities of intermolecular interactions (hydrogen bonds). In the aqueous medium, there are strong interactions between the H_2O molecules, as a result of the difference in electronegativity of H and O atoms. These hydrogen bonds are highly polar, leading to the strong bonds of two hydrogen atoms (H δ^+) (belonging to one H_2O molecule) with other two H_2O molecules. In another bond mechanism, the oxygen atom (O δ^-) (having two free electron pairs) of each H_2O molecule is able to interact with the H atoms of other neighboring H_2O molecules[98,99] (green dotted circle in Fig. 8(b)). There are exactly the correct number of δ^+ hydrogens and lone pairs so that each of them can be involved in hydrogen bonds.[100,101]

In the second case (Fig. 8(c)), there are also the presence of H bonds in the $C_3H_8O_2$ solvents because the hydrophilic characteristics, *i.e.*, the degree of polarity between the O δ^- and H δ^+ atoms associated to the two hydroxyl (OH) groups. However, each $C_3H_8O_2$ molecule forms six H bonds with other $C_3H_8O_2$ molecules located near its neighborhood.[102–104]

The syntheses performed in H_2O solution favored the precipitation of $CaWO_4$ crystals, while those in $C_3H_8O_2$ solvent resulted in a stable colloid suspension. After the solutions were prepared, they were transferred inside the Teflon autoclave (Fig. 8(d)), which was placed inside the domestic microwave-hydrothermal system. Basically, this apparatus was developed by means of several adaptations performed on a microwave oven (model NN-ST357WRPH Piccolo 22 L, Panasonic).[105] Inside this system, the high microwave frequency interacts with the permanent dipoles of the liquid phase (H_2O or $C_3H_8O_2$), initiating a rapid heating *via* molecular rotation. Likewise, the permanent or induced dipoles in the dispersed phase cause

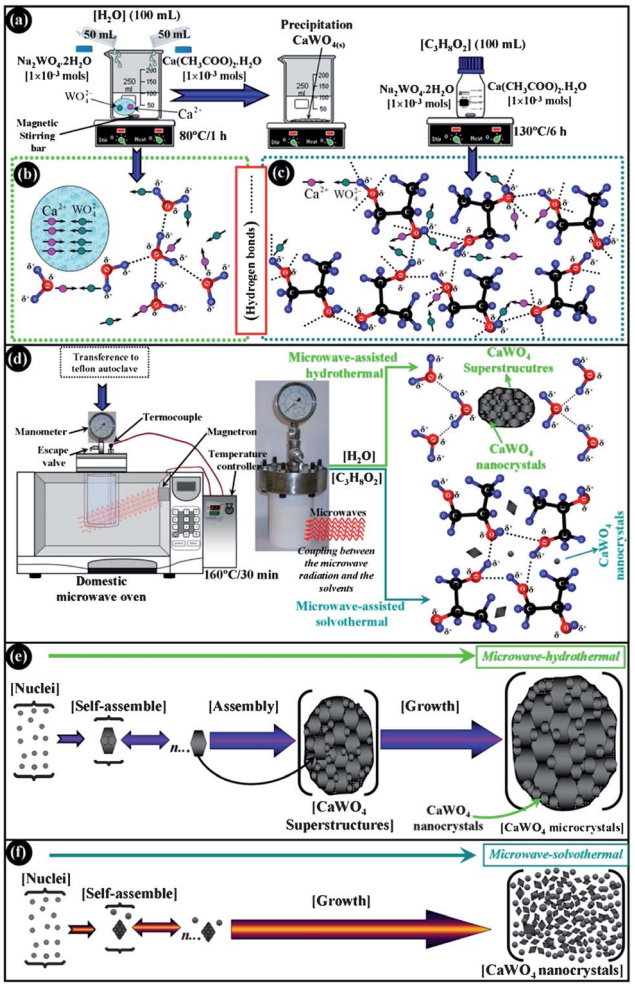

Fig. 8 (a) Schematic representation of the experimental procedure employed in the co-precipitation reaction using H_2O and $C_3H_8O_2$ as solvents; (b) electrostatic attraction of Ca^{2+} and WO_4^{2-} ions in solution and possible interactions between the H_2O molecules; (c) probable interactions between the $C_3H_8O_2$ molecules; (d) illustration of the domestic microwave-assisted hydrothermal system employed in the processing of $CaWO_4$ crystals and adsorption process of H_2O or $C_3H_8O_2$ on the crystal surfaces; (e,f) proposed growth mechanisms for the aggregated $CaWO_4$ micro- and nanocrystals processed in MH and MS, respectively.

a rapid heating of the particles.[106,107] The microwave radiation also promotes an increase in the effective collision rate between the particles in suspension, contributing to the crystal attachment and growth processes. The adsorption of H_2O or $C_3H_8O_2$ on the $CaWO_4$ surfaces favor the aggregation of particles, keeping adhered by van der Waals forces. Fig. 8(e,f) show a proposed growth mechanism responsible for the formation and growth of aggregated $CaWO_4$ crystals. Considering the MH conditions, after formation of the first nuclei, self-organization and/or mutual aggregation occurs between them by uncountable collision events. The self-assembly mechanism is controlled by particle–particle interactions (*n*…units) followed by the coalescence of octahedron-like $CaWO_4$ nanocrystals. The growth and agglomeration of these nanocrystals are the origin of the complex superstructures (Fig. 8(e)). These results are in agreement with

Published on 18 November 2011 on http://pubs.rsc.org | doi:10.1039/C1CE05977G
Downloaded by UNIVERSIDAD SAO PAULO on 07 February 2012

Published on 18 November 2011 on http://pubs.rsc.org | doi:10.1039/C1CE05977G
Downloaded by UNIVERSIDAD SAO PAULO on 07 February 2012

the explanations recently reported by Tian *et al.*[108] Fig. 8(f) illustrates the growth mechanism of $CaWO_4$ nanocrystals under MS treatment. In this second situation involving the $C_3H_8O_2$ as solvent, the formation of the first $CaWO_4$ nuclei is slower than in the aqueous medium due to the high viscosity to reduce the diffusion rate of Ca^{2+} and WO_4^{2-} ions. After this stage, these nuclei aggregate and coalesce as similar as in the MH environment. However, the adsorption of $C_3H_8O_2$ molecules on the inorganic surfaces of $CaWO_4$ nanocrystals minimizes the particle–particle interaction by steric effects. On the other hand, as it is impossible to completely avoid the contact of nanoparticles (*n*…units) in suspension, small groups of aggregated particles are formed in this system (Fig. 7(e,f)). Subsequently, the heating promoted by the microwave radiation contributes to the growth of these nanocrystals.

Ultraviolet-visible absorption spectroscopy and band structures analyses of $CaWO_4$ crystals

The optical band gap energy (E_{gap}) was calculated by the method proposed by Kubelka and Munk.[109] This methodology is based on the transformation of diffuse reflectance measurements to estimate the E_{gap} values with good accuracy.[110] Particularly, it can be well-employed in limited cases of infinitely thick sample layer. The Kubelka–Munk equation for any wavelength is described as:

$$F(R_\infty) = \frac{(1 - R_\infty)^2}{2R_\infty} = \frac{k}{s} \quad (8)$$

where $F(R_\infty)$ is the Kubelka–Munk function or absolute reflectance of the sample. In our case, the magnesium oxide (MgO) was the standard sample in the reflectance measurements. $R_\infty = R_{sample}/R_{MgO}$ (R_∞ is the reflectance when the sample is infinitely thick), k is the molar absorption coefficient, and s is the scattering coefficient.

In a parabolic band structure, the optical band gap and absorption coefficient of semiconductor oxides[111] can be calculated by the following equation:

$$\alpha hv = C_1(hv - E_{gap})^n, \quad (9)$$

where α is the linear absorption coefficient of the material, hv is the photon energy, C_1 is a proportionality constant, E_{gap} is the optical band gap and n is a constant associated to the different kinds of electronic transitions ($n = 0.5 \rightarrow$ direct allowed, $n = 2 \rightarrow$ indirect allowed, $n = 1.5 \rightarrow$ direct forbidden and $n = 3 \rightarrow$ indirect forbidden). According to the literature, the tungstates (AWO_4; A = Ca, Sr, Ba) exhibit an optical absorption spectrum governed by direct electronic transitions.[112] In this phenomenon, after electronic absorption process, the electrons located in the maximum-energy states in the valence band fall back to the minimum-energy states in the conduction band under the same point in the Brillouin zone.[113] Based on this information, the E_{gap} values of $CaWO_4$ crystals were calculated using $n = 0.5$ in eqn (9). Finally, using the remission function described in eqn (8) and with the term $k = 2\alpha$ and C_2 is a proportionality constant, we obtain the modified Kubelka–Munk equation as indicated in eqn (10):

$$[F(R_\infty)hv]^2 = C_2(hv - E_{gap}), \quad (10)$$

Therefore, finding the $F(R_\infty)$ value from eqn (10) and plotting a graph of $[F(R_\infty)hv]^2$ against hv it was possible determine the E_{gap} of $CaWO_4$ nanocrystals.

Fig. 9(a–e) illustrate the band structures and UV-vis spectra of $CaWO_4$ crystals processed in MH and MS systems.

Fig. 9(a–c) revealed that the band structures of all $CaWO_4$ crystals are characterized by well-defined direct electronic transitions, which is typical nature of crystalline semiconductor materials. Fundamentally, the top of the valence band (VB) as well as the bottom of the conduction band (CB) are in a same Γ point. In these figures, we verify that the theoretical band gap values are close to those experimentally estimated by the UV-vis spectra (Fig. 9(d,e)).

The exponential optical absorption edge and the optical band gap energy are controlled by the degree of structural disorder in the lattice. The decreasing in the E_{gap} can be attributed to the existence of defects, local bond distortion, intrinsic surface states and interfaces, which yield localized electronic levels within the forbidden band gap.[114,115] For a simplified description, we believe that these differences in the E_{gap} values are mainly attributed to the distortions on both $[CaO_8]$ and $[WO_4]$ clusters at short and medium-range.

Considering these results, it is assumed that the $CaWO_4$ nanocrystals (lower band gap) are more disordered than the microcrystals (Fig. 9(d,e)). The previous analyses based on the Rietveld refinements indicated that the $[WO_4]$ clusters are well-distorted in the nanocrystals. It is clear that this disorder propagates at medium-range by the interaction between clusters. Consequently, this distortion process on the fundamental $[WO_4]_d$ and $[CaO_8]_d$ clusters favors the formation of intermediary energy levels above the VB and below the CB, conferring a reduction in the band gap of the material.

Density of states of $CaWO_4$ crystals

Fig. 10(a–c) show the electronic diagrams, illustrating the density of states (DOS) for the theoretical optimized structure and for those of $CaWO_4$ micro- and nanocrystals, respectively.

The ability of improving the properties and the performance of materials is fundamentally dependent on the detailed knowledge between the electronic structure and microstructure. A considerable reduction in the E_{gap} of $CaWO_4$ micro- and nanocrystals was observed when compared to the optimized model in Fig. 10 (a). Basically, it is resulting from different numbers of occupied states or distinct organizations of intermediary energy levels within the band gap, as a consequence of the distortions on the $[CaO_8]$ and $[WO_4]$ clusters. The DOS projected on the atoms and orbitals for the optimized model and for the nanocrystals indicated that the VB maximum is derived from O2p ($2p_x$, $2p_y$ and $2p_z$) orbitals. On the other hand, the CB is composed of two arrangements of hybrid orbitals, the first one is formed of $W5dp_{xz}$, $5dp_{xy}$ and $5dp_{yz}$ orbitals while the second one is constituted of $W5d_{z^2}$ and $5d_{x^2-y^2}$ orbitals (Fig. 10(a,b)). An examination more detailed of the DOS results demonstrated a high contribution in the CB of $W5d_{xz}$, $5d_{xy}$ and $5d_{yz}$ orbitals than those $W5d_{z^2}$ and $5d_{x^2-y^2}$ orbitals for the aggregated $CaWO_4$

 This journal is © The Royal Society of Chemistry 2012

Published on 18 November 2011 on http://pubs.rsc.org | doi:10.1039/C1CE05977G
Downloaded by UNIVERSIDAD SAO PAULO on 07 February 2012

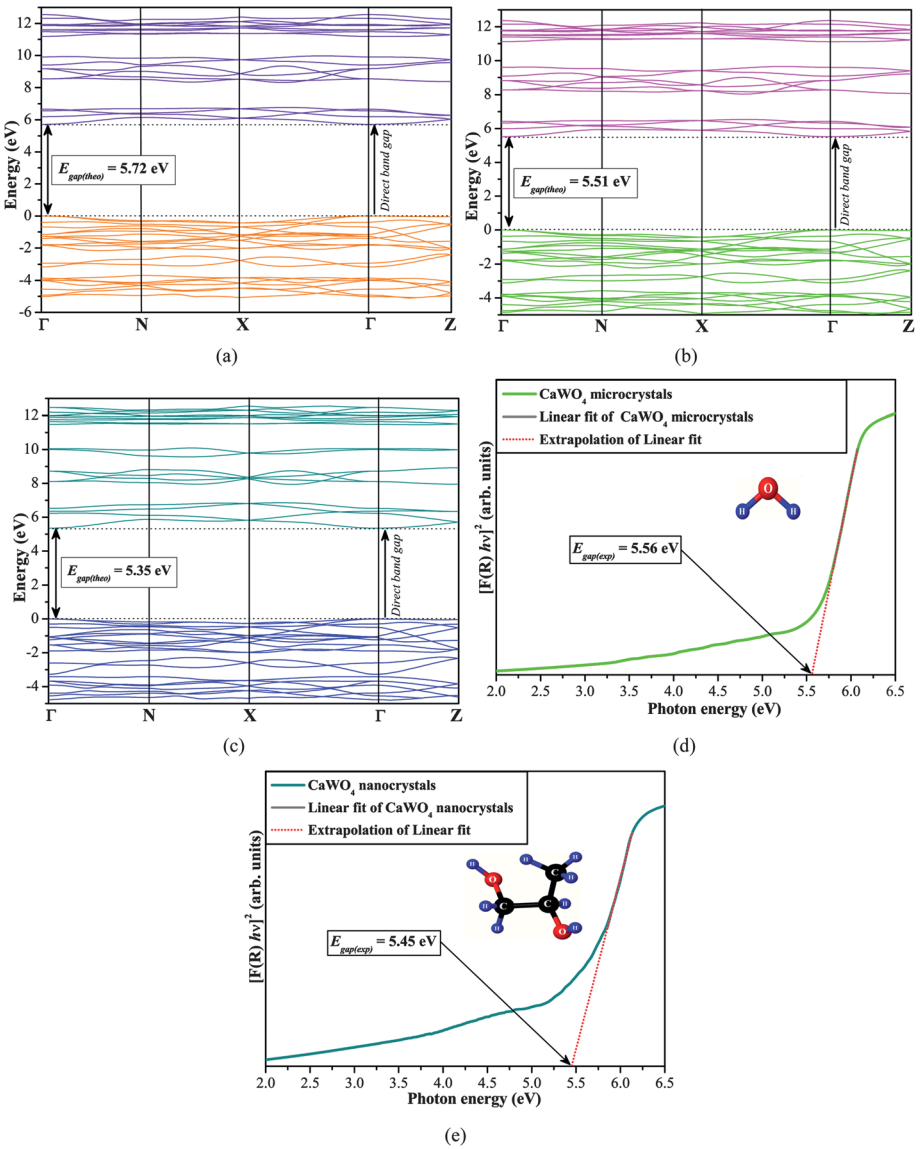

Fig. 9 Calculated band structures for the: (a) optimized model, (b) $CaWO_4$ microcrystals and (c) nanocrystals; (d,e) UV-vis spectra of aggregated $CaWO_4$ micro- and nanocrystals processed in MH and MS, respectively.

microcrystals. The opposite situation was evidenced for the nanocrystals, *i.e.*, the predominance in the CB of W5d_{z^2} and 5$d_{x^2-y^2}$ orbitals.

The analysis performed on the site- and orbital-resolved DOS denoted a significant dependence of W orbitals in the CB. In general, we presume that this behavior can be correlated with the distortions on the $[WO_4]_d$ clusters within the scheelite structure, which are responsible for the origin of intermediary energy levels located above the CB. The theoretical results indicated that the $CaWO_4$ nanocrystals have a more disordered structure as well as a high degree of distorted $[WO_4]_d$ clusters. In other words, the aggregate $CaWO_4$ microcrystals have a high degeneracy split of orbitals. These effects led to the modification in the electronic structure of both $CaWO_4$ nano- and microcrystals due to the local (intracluster) and medium disorders (intercluster) in the quantum domain.

Thus, assuming a free density of electronic states in the periodic potential of an extended solid, the energy and crystal momentum can be both precisely defined, except for the position. For a localized density of electronic states the energy may be well-defined, but the uncertainty in the position decreases, and then the momentum can not be exactly defined. The discrete energy of the particle eigenfunctions can be understood as localized electronic levels within the forbidden band gap. Due to the increase of distortions on the clusters, the orbitals become more delocalized as a condition imposed by the Heisenberg's uncertainty principle. In quantum mechanics, this principle explains that the physical properties as position and momentum can not be simultaneously known with high precision.

The polarization between the $[WO_4]_d$ and $[CaO_8]_d$ clusters and the changes of electronic transition directly influence the physical properties (for example, the photoluminescence) of the scheelites. Hence, the intrinsic PL emissions can be attributed to these mechanisms, which are derived from interactions between distorted $[WO_4]_d$ and $[CaO_8]_d$ pre-existing clusters.

Published on 18 November 2011 on http://pubs.rsc.org | doi:10.1039/C1CE05977G
Downloaded by UNIVERSIDAD SAO PAULO on 07 February 2012

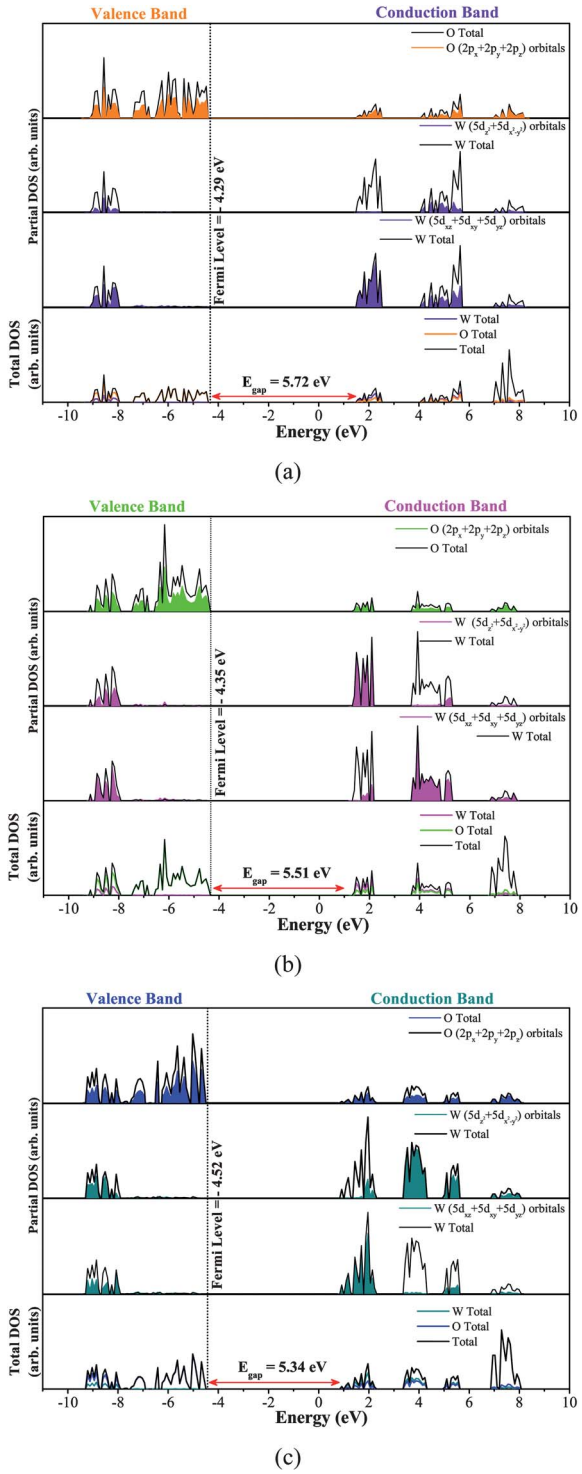

Fig. 10 Total DOS of crystalline structure for the: (a) optimized model, (b) $CaWO_4$ microcrystals and (c) nanocrystals.

Photoluminescence emissions of $CaWO_4$ crystals

Fig. 11 illustrates the PL spectra at room temperature of aggregated $CaWO_4$ micro- and nanocrystals processed in MH and MS. Insets show the digital photographs of PL emissions of these crystals.

The PL profiles have a typical behavior of multiphonon or multilevel processes, *i.e.*, a solid system in which the relaxation occurs by several paths, involving the participation of numerous energy states within the band gap. The PL emission spectra of tungstates are frequently decomposed into blue, green and red light components.[24] However, there are many controversial interpretations with regard to the blue and green maximum PL emissions of these materials. Blasse and Wiegel[116] and Korzhik *et al.*[117] concluded that the green emissions arise from WO_3 centers. Sokolenko *et al.*[118] attributed to the green–red emission of $WO_3 \cdot \ddot{V}_O$ oxygen-deficient complexes. Sienelnikov *et al.*[119] suggested that the distorted tetrahedral $[WO_4]$ clusters cause the formation of oxygen vacancies, resulting in the green luminescence band. In general, it is assumed that the emission spectra of $CaWO_4$ crystals are associated to the charge-transfer transitions within the $[WO_4]^{2-}$ complexes[120–123] or due to the vacancies as $[WO_3 \cdot V_O^z]$[24,124,125] and $[CaO_7 \cdot V_O^z]$[24] (where $V_O^z = V_O^z$, $\dot{V}_O$, or $\ddot{V}_O$).

The PL spectra of aggregated $CaWO_4$ nano- and microcrystals revealed an intense blue luminescence emission. The broad luminescence is a response to the numerous kinds of extrinsic and intrinsic defects directly associated to the degree of structural order–disorder. The variations on the density of structural defects are responsible for the shift observed in the maximum PL emission point (491 nm and 484 nm for the $CaWO_4$ micro- and nanocrystals, respectively).

In a typical semiconductor, the intercluster (intermediary range) and intracluster (local range) interaction can be due to the three different sources: orientation, induction and dispersion interactions. The orientation interaction is associated with the correlation between the rotation motion of the permanent moments in different $[WO_4]$–$[WO_4]$, $[CaO_8]$–$[CaO_8]$ or $[WO_4]$–$[CaO_8]$ complex clusters (medium-range). The induction interaction occurs *via* polarization processes of $[CaO_8]$ or $[WO_4]$ clusters by the permanent moment of another neighbor $[WO_4]$ or $[CaO_8]$ clusters (short-range). The dispersion interaction arises from the correlation between the electrons situated in the neighborhood of $[WO_4]$ or $[CaO_8]$ clusters (long-range).

Theoretical results have shown that the symmetry break process (effect of order–disorder) in the structure of various

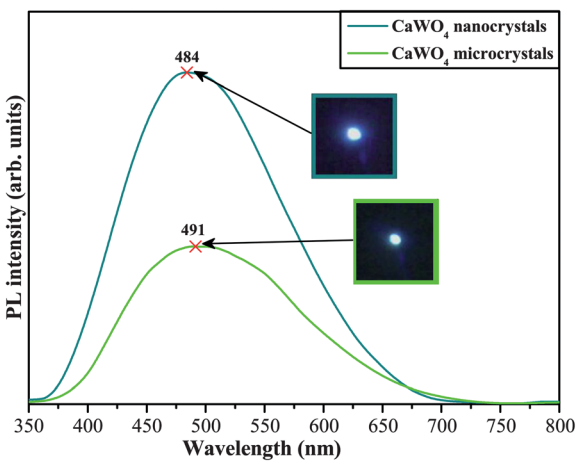

Fig. 11 PL spectra of aggregated $CaWO_4$ micro- and nanocrystals processed in MH and MS, respectively.

This journal is © The Royal Society of Chemistry 2012

Table 5 Comparative results between the luminescence lifetime and quantum yield of $CaWO_4$ micro- and nanocrystals obtained in this work with those published in the literature

Samples	A_1	τ	Quantum yield (%)	λ_{exc}/nm	Ref.
$CaWO_4:Tm^{3+}$ microcrystals	342	1.53 μs	—	394	13
$CaWO_4:Eu^{3+}$ nanocrystals	—	0.969 ms	92	365	62
$CaWO_4:Tb^{3+}$ microcrystals	—	1.024 ms	—	254	132
$CaWO_4$ microcrystals	8167	1.9 μs	5.8	350	[✠]
$CaWO_4$ nanocrystals	15862	4.05 μs	11.4	350	[✠]

Published on 18 November 2011 on http://pubs.rsc.org | doi:10.1039/C1CE05977G
Downloaded by UNIVERSIDAD SAO PAULO on 07 February 2012

semiconductors is a necessary condition for the existence of intermediary energy levels within the forbidden band gap.[126,127] These structural changes are related to the charge polarization at short and medium-range, which can be manifestations of quantum confinement (independently of the particle size). The key point of quantum confinement is the presence of discrete energy levels within the band gap, which are not possible for a periodic crystal at long, medium and short range.

The cluster-to-cluster charge-transfer (CCCT) in a crystal, containing more than one kind of cluster, is characterized by excitations involving electronic transitions from one cluster to another. Longo *et al.*[33] demonstrated that the CCCT mechanism in hierarchical assemblies of $CaMoO_4$ ($[MoO_4]^x$–$[MoO_3\cdot V_O^z]$ or $[CaO_8]^x$–$[CaO_7\cdot V_O^z]$) and $[(MoO_4]'$ –$[MoO_3\cdot \dot{V}_O]$ or $(CaO_8]'$–$[CaO_7\cdot \dot{V}_O]$) can be considered a new class of electronic transitions involved during the PL emissions. In this work, we consider that within the $CaWO_4$ lattice, the $[WO_4]_o^x$–$[WO_4]_d^x$ and/or $[CaO_8]_o^x$–$[CaO_8]_d^x$ (o = ordered; d = distorted) clusters arise from structural distortions, where it is possible for electronic transference to occur between them. Therefore, these $[WO_4]_o^{'}$–$[WO_4]_d^{\cdot}$ and/or $[CaO_8]_o^{'}$–$[CaO_8]_d^{\cdot}$ clusters present extrinsic defects, which are linked to the effects of order–disorder in the electronic structure, surfaces and interfaces, commonly verified in materials with scheelite-type structure synthesized in the MH method.[128,129] These defects create additional energy states above the VB and below the CB, decreasing the band gap.[30,33]

The structural and electronic reconstructions of all possible combinations of clusters belonging to a specific crystal are essential for the understanding of the CCCT process and its influences on the PL phenomenon. In this case, the increase in the band gap (as shown by the UV-vis measurements) promotes a formation of intermediary levels (deep defects) and a shift from blue to cyan PL emissions as a response to the increase of crystal size. In the photoinduced charge-transfer process, the electrons are promoted from occupied levels of donor clusters to empty levels of receptor clusters. The formation of isolated energy levels (quantum confinement) and the presence of distorted $[WO_4]_d^{\cdot}$ and/or $[CaO_8]_d^{\cdot}$ clusters cause a substantial recombination between the photoexcited electron and hole during the excitation processes. Probably, the $[WO_4]_o^x$–$[WO_4]_d^x$ and/or $[CaO_8]_o^x$–$[CaO_8]_d^x$ clusters are activated during the excitation process, changing its symmetry to singlet or triplet states, as demonstrated by Gracia *et al.*[130] for the $CaWO_4$ structure. Thus, similar studies need to be done for the materials with scheelite-type structure in order to confirm this scientific fact.

Finally, we have calculated the luminescence lifetime for the maximum emission, which were measured under the excitation wavelength at 350 nm. Therefore, we have applied in exponential decay curve deviate a fit adjust with first-order kinetics (Supporting information Fig. SI-4(a,b)†). These exponential decay curves can be well fitted into a single-exponential function as shown in eqn (11):[131]

$$I = I_0 + A_1\exp(-t/\tau), \quad (11)$$

where, I and I_0 are PL intensity, A is the amplitude, t is the asymptotic value to fitting curves and τ is the luminescent lifetimes. Moreover, on the basis of emission spectra (Fig. 11) and the lifetimes of maximum PL emission, the quantum efficiency (η) of aggregated $CaWO_4$ micro- and nanocrystals processed in MH and MS can be determined, according to the literature.[62] We have assumed, that only nonradiative and radiative processes are involved in the depopulation of maximum PL emission. The fitting parameters for lifetimes and quantum yield are listed in Table 5.

As it can be seen from Table 5, the average lifetimes and quantum efficiencies of rare-earth doped $CaWO_4$ crystals are in general higher than our pure $CaWO_4$ micro- and nanocrystals.[13,62,132] This behavior, can be related to the presence of defects in the lattice caused by microwave irradiation. Moreover, we have noted that during the excitation process a decay in intensity of PL emission occurs in our crystals. Therefore, the intensity of PL emission (lifetimes and quantum yield) is probably related to the level of structural organization, which can be modeled by synthesis methods and thermal treatment conditions.

Conclusions

In summary, aggregated $CaWO_4$ micro- and nanocrystals were obtained by the microwave-assisted hydrothermal/solvothermal method at 160 °C for 30 min. XRD patterns showed that the $CaWO_4$ crystals have a scheelite-type tetragonal structure with space group $I4_1/a$. The $CaWO_4$ crystals synthesized by the MS method exhibited a microstrain broadening of diffraction peaks due the presence of nanocrystals. The changes in the atomic positions of oxygen atoms evidenced in the Rietveld refinements indicate significant distortions on the $[CaO_8]$ and $[WO_4]$ clusters. The Raman-active modes proved the existence of local order at short-range for both nano- and microcrystals. The IR-active modes revealed a typical stretching and/or bending vibrations of $[WO_4]$ and $[CaO_8]$ clusters. Moreover, the relative positions of experimental Raman and IR-active modes were corroborated with those theoretically calculated. FE-SEM and TEM images showed the formation of aggregated $CaWO_4$ microcrystals with

Published on 18 November 2011 on http://pubs.rsc.org | doi:10.1039/C1CE05977G
Downloaded by UNIVERSIDAD SAO PAULO on 07 February 2012

polydisperse particle size distribution. These microcrystals are composed of several nanocrystals, where some of them are attached in similar crystallographic orientations. On the other hand, the MS resulted in the origin of uncountable aggregated octahedron-like nanocrystals. In this case, the viscosity as well as the adsorption of $C_3H_8O_2$ molecules on the particle surfaces inhibited the growth and reduced the particle–particle interactions in this medium. The different E_{gap} values between the micro- and nanocrystals were attributed to the existence of localized electronic levels within the forbidden band gap. We conclude that these energy states specially derive from distortions on both $[WO_4]$ and $[CaO_8]$ clusters at short and medium-range. The theoretical calculation indicated that the band structures of all $CaWO_4$ crystals are characterized by direct electronic transitions. According to the DOS analyses, the energy states in the VB is constituted from ($O2p_x$, $2p_y$, and $2p_z$) orbitals, while in the CB there is the contribution of two distinct groups of W orbitals ($W5d_{xz}$, $5d_{xy}$, $5d_{yz}$ between the axes) and ($W5d_{z^2}$, $5d_{x^2-y^2}$ orbitals on the axis). In the nanocrystals formed by the MS, the CB has a higher predominance of $W5d_{z^2}$ and $W5d_{x^2-y^2}$ orbitals than those of $W5d_{xz}$, $5d_{xy}$, and $5d_{yz}$. The inverse condition was observed for the microcrystals obtained under MH treatment. The maximum PL emissions at 491 nm and 484 nm for the $CaWO_4$ micro- and nanocrystals were attributed to the CCCT mechanism involved in the electronic transitions between $[WO_4]_o^x$–$[WO_4]_d^x$ or $[CaO_8]_o^x$–$[CaO_8]_d^x$ and $[WO_4]_o^{'}$–$[WO_4]_d^{'}$ and/or $[CaO_8]_o^{'}$–$[CaO_8]_d^{'}$ clusters. The highest lifetime and quantum yield were observed for $CaWO_4$ nanocrystals.

Acknowledgements

The authors thank the financial support of the Brazilian research financing institutions: FAPESP (No. 2009/50303-4/53189-8/2008/55585-5), CNPq and CAPES. Special thanks to Prof. Dr D. Keyson and Dr D.P. Volanti by the development of the microwave-hydrothermal system.

References

1 G. Jia, C. Wang and S. Xu, *J. Phys. Chem. C*, 2010, **114**, 17905.
2 X. Yan-Ling, Z. Hong, W. Rui and Z. Chun-Yu, *Chin. Phys. Lett.*, 2011, **6**, 064210.
3 H. Lei, S. Zhang, X. Zhu, Y. Sun and Y. Fu, *Mater. Lett.*, 2010, **64**, 344.
4 D. Errandonea, R. S. Kumar, X. Ma and C. Tu, *J. Solid State Chem.*, 2008, **181**, 355.
5 V. I. Balakshy, K. R. Asratyan and V. Y. Molchanov, *J. Opt. A: Pure Appl. Opt.*, 2001, **3**, S87.
6 L. Fan, Y. X. Fan, Y. H. Duan, Q. Wang, H. T. Wang, G. H. Jia and C. Y. Tu, *Appl. Phys. B: Lasers Opt.*, 2009, **94**, 553.
7 J. Sulc, H. Jelinkova, T. T. Basiev, M. E. Doroschenko, L. I. Ivleva, V. V. Osiko and P. G. Zverev, *Opt. Mater.*, 2007, **30**, 195.
8 P. G. Yang, J. Liu, H. Yang, X. Yu, Y. Guo, Y. Zhou and J. Liu, *J. Mater. Chem.*, 2009, **19**, 3771.
9 J. Bi, L. Wu, Y. Zhang, Z. Li, J. Li and X. Fu, *Appl. Catal., B*, 2009, **91**, 135.
10 J. Yu, L. Qi, B. Cheng and X. Zhao, *J. Hazard. Mater.*, 2008, **160**, 621.
11 J. Liu, H. Lian and C. Shi, *Opt. Mater.*, 2007, **29**, 1591.
12 J. Liao, B. Qiu, H. Wen, J. Chen and W. You, *Mater. Res. Bull.*, 2009, **44**, 1863.
13 J. Liao, B. Qiu, H. Wen, J. Chen, W. You and L. Liu, *J. Alloys Compd.*, 2009, **487**, 758.
14 A. V. Veresnikova, B. K. Lubsandorzhiev, I. R. Barabanov, P. Grabmayr, D. Greiner, J. Jochum, M. Knapp, C. Ostwald, R. V. Poleshuk, F. Ritter, B. A. M. Shaibonov, Y. E. Vyatchin and G. Meierhofer, *Nucl. Instrum. Methods Phys. Res., Sect. A*, 2009, **603**, 529.
15 V. B. Mikhailika, S. Henrya, H. Krausa and I. Solskii, *Nucl. Instrum. Methods Phys. Res., Sect. A*, 2007, **583**, 350.
16 I. Annenkov, O. A. Buzanov, F. A. Danevich, A. Sh. Georgadze, S. K. Kim, H. J. Kim, Y. D. Kim, V. V. Kobychev, V. N. Kornoukhov, M. Korzhik, J. I. Lee, O. Missevitch, V. M. Mokina, S. S. Nagorny, A. S. Nikolaiko, D. V. Poda, R. B. Podviyanuk, D. J. Sedlak, O. G. Shkulkova, J. H. So, I. M. Solsky, V. I. Tretyak and S. S. Yurchenko, *Nucl. Instrum. Methods Phys. Res., Sect. A*, 2008, **584**, 334.
17 G. K. Choi, J. R. Kim, S. H. Yoon and K. S. Hong, *J. Eur. Ceram. Soc.*, 2007, **27**, 3063.
18 G.-K. Choi, S.-Y. Cho, J.-S. An and K. S. Hong, *J. Eur. Ceram. Soc.*, 2006, **26**, 2011.
19 H. Kraus and V. B. Mikhailik, *Nucl. Instrum. Methods Phys. Res., Sect. A*, 2010, **621**, 395.
20 J. Ninkovic, G. Angloher, C. Bucci, C. Cozzini, T. Frank, D. Hauff, H. Kraus, B. Majorovits, V. Mikhailik, F. Petricca, F. Probst, Y. Ramachers, W. Rau, W. Seidel and S. Uchaikin, *Nucl. Instrum. Methods Phys. Res., Sect. A*, 2005, **537**, 339.
21 I. Trabelsi, M. Dammak, R. Maalej and M. Kamoun, *Phys. B*, 2011, **406**, 315.
22 W. Wang, P. Yang, S. Gai, N. Niu, F. He and J. Lin, *J. Nanopart. Res.*, 2010, **12**, 2295.
23 Q. Xiao, Q. Zhou and M. Li, *J. Lumin.*, 2010, **130**, 1092.
24 A. B. Campos, A. Z. Simões, E. Longo, J. A. Varela, V. M. Longo, A. T. de Figueiredo, F. S. De Vicente and A. C. Hernandes, *Appl. Phys. Lett.*, 2007, **91**, 051923.
25 Q. Zhang, W.-T. Yao, X. Chen, X. Zhu, Y. Fu, G. Zhang, L. Sheng and S.-H. Yu, *Cryst. Growth Des.*, 2007, **7**, 1423.
26 A. Phuruangrat, T. Thongtem and S. Thongtem, *J. Exp. Nanosci.*, 2010, **5**, 263.
27 T. Thongtem, A. Phuruangrat and S. Thongtem, *Appl. Surf. Sci.*, 2008, **254**, 7581.
28 E. Orhan, M. Anicete-Santos, M. A. M. A. Maurera, F. M. Pontes, A. G. Souza, J. Andrés, A. Beltran, J. A. Varela, P. S. Pizani, C. A. Taftf and E. Longo, *J. Solid State Chem.*, 2005, **178**, 1284.
29 W. Hu, W. Tong, L. Li, J. Zheng and G. Li, *Phys. Chem. Chem. Phys.*, 2011, **13**, 11634.
30 L. S. Cavalcante, J. C. Sczancoski, J. W. M. Espinosa, J. A. Varela, P. S. Pizani and E. Longo, *J. Alloys Compd.*, 2009, **474**, 195.
31 T. K. Thirumalaisamy and R. J. Saravanan, *J. Mater. Sci.: Mater. Electron.*, 2011, **22**, 1637.
32 L. S. Cavalcante, J. C. Sczancoski, V. C. Albarici, J. M. E. Matos, J. A. Varela and E. Longo, *Mater. Sci. Eng., B*, 2008, **150**, 18.
33 V. M. Longo, L. S. Cavalcante, E. C. Paris, J. C. Sczancoski, P. S. Pizani, M. S. Li, J. A. Andrés, E. Longo and J. A. Varela, *J. Phys. Chem. C*, 2011, **115**, 5207.
34 V. M. Longo, A. T. de Figueiredo, A. B. Campos, J. W. M. Espinosa, A. C. Hernandes, C. A. Taft, J. R. Sambrano, J. A. Varela and E. Longo, *J. Phys. Chem. A*, 2008, **112**, 8920.
35 J. C. Sczancoski, L. S. Cavalcante, N. L. Marana, R. O. da Silva, R. L. Tranquilin, M. R. Joya, P. S. Pizani, J. A. Varela, J. R. Sambrano, M. S. Li, E. Longo and J. Andrés, *Curr. Appl. Phys.*, 2010, **10**, 614.
36 V. S. Marques, L. S. Cavalcante, J. C. Sczancoski, A. F. P. Alcântara, M. O. Orlandi, E. Moraes, E. Longo, M. S. Li and M. R. M. C. Santos, *Cryst. Growth Des.*, 2010, **10**, 4752.
37 Z. Luo, H. Li, J. Xi, W. Zhu, J. Guo and B. Zhang, *J. Cryst. Growth*, 2007, **300**, 523.
38 Z. Luo, H. Li, J. Xia, W. Zhu, J. Guo and B. Zhang, *Mater. Lett.*, 2007, **61**, 1845.
39 Y. Yin and A. P. Alivisatos, *Nature*, 2005, **437**, 664.
40 S. Komarneni and H. Katsuki, *Pure Appl. Chem.*, 2002, **74**, 1537.
41 S. Komarneni, V. C. Menon, Q. H. Li, R. Roy and F. Ainger, *J. Am. Ceram. Soc.*, 1996, **79**, 1409.
42 S. Komarneni, R. Roy and Q. H. Li, *Mater. Res. Bull.*, 1992, **27**, 1393.
43 C. O. Kappe, A. Stadler, *Microwave organic and medicinal chemistry*, Willey. Vol. 25, 2001, p. 12–20.
44 T. Thongtem, A. Phuruangrat and S. Thongtem, *Curr. Appl. Phys.*, 2008, **8**, 189.
45 J. Bi, L. Wu, Z. Li, Z. Ding, X. Wang and X. Fu, *J. Alloys Compd.*, 2009, **480**, 684–688.

 This journal is © The Royal Society of Chemistry 2012

View Online

Downloaded by UNIVERSIDAD SAO PAULO on 07 February 2012
Published on 18 November 2011 on http://pubs.rsc.org | doi:10.1039/C1CE05977G

46 M. L. Moreira, D. P. Volanti, J. Andrés, P. J. R. Montes, M. E. G. Valerio, J. A. Varela and E. Longo, *Scr. Mater.*, 2011, **64**, 118.
47 R. Dovesi, V. R. Saunders, C. Roetti, R. Orlando, C. M. Zicovich-Wilson, F. Pascale, B. Civalleri, K. Doll, N. M. Harrison, I. J. Bush, P. D. Arco, M. Llunell, *CRYSTAL06 Users Manual*, University of Torino, 2006.
48 A. D. Becke, *J. Chem. Phys.*, 1993, **98**, 5648.
49 C. Lee, W. Yang and R. G. Parr, *Phys. Rev. B*, 1988, **37**, 785.
50 F. Corà, M. Alfredsson, G. Mallia, D. S. Middlemiss, W. Mackrodt, R. Dovesi, R. Orlando, *Structure and Bonding*, Springer-Verlag, Berlin, 2004. p. 113.
51 H. J. Monkhorst and J. C. Pack, *Phys. Rev. B: Solid State*, 1976, **13**, 5188.
52 (*a*) A. Kokalj, *J. Mol. Graphics Modell.*, 1999, **17**, 176; (*b*) http://www.crystal.unito.it/Basis_Sets.
53 R. D. Burbank, *Acta Crystallogr.*, 1965, **18**, 88.
54 A. P. A. Marques, F. C. Picon, D. M. A. Melo, P. S. Pizani, E. R. Leite, J. A. Varela and E. Longo, *J. Fluoresc.*, 2007, **18**, 51.
55 M. Maczka, K. Hermanowicz, P. E. Tomaszewski, M. Zawadzki and J. Hanuza, *Solid State Sci.*, 2008, **10**, 61.
56 H. M. Rietveld, *Acta Cryst.*, 1967, **2**, 65.
57 http://www.ing.unitn.it/~maud/.
58 L. Lutterotti, S. Matthies, H. R. Wenk, A. J. Schultz and J. J. Richardson, *J. Appl. Phys.*, 1997, **81**, 594.
59 E. Cavalli, P. Boutinaud, R. Mahiou, M. Bettinelli and P. Dorenbos, *Inorg. Chem.*, 2010, **49**, 4916.
60 S. K. Arora and B. Chudasama, *Cryst. Res. Technol.*, 2006, **41**, 1089.
61 D. Errandonea, J. Pellicer-Porres, F. J. Manjón, A. Segura, C. Ferrer-Roca, R. S. Kumar, O. Tschauner, P. Rodríguez-Hernández, J. López-Solano, S. Radescu, A. Mujica, A. Muñoz and G. Aquilanti, *Phys. Rev. B: Condens. Matter Mater. Phys.*, 2005, **72**, 174106.
62 Y. Su, L. Li and G. Li, *Chem. Mater.*, 2008, **20**, 6060.
63 L. S. Cavalcante, J. C. Sczancoski, L. F. Lima, Jr., J. W. M. Espinosa, P. S. Pizani, J. A. Varela and E. Longo, *Cryst. Growth Des.*, 2009, **9**, 1002.
64 (*a*) J. C. Sczancoski, L. S. Cavalcante, M. R. Joya, J. W. M. Espinosa, P. S. Pizani, J. A. Varela and E. Longo, *J. Colloid Interface Sci.*, 2009, **330**, 227; (*b*) L. Li, Y. Su and G. Li, *Appl. Phys. Lett.*, 2007, **90**, 054105.
65 S. R. Hall, F. H. Allen and I. D. Brown, *Acta Crystallogr., Sect. A: Found. Crystallogr.*, 1991, **47**, 655.
66 D. L. Bish and J. E. Post, *Am. Min*, 1993, **78**, 932.
67 M. Ferrari and L. Lutterotti, *J. Appl. Phys.*, 1994, **76**, 7246.
68 http://ftp.ccp14.dl.ac.uk/ccp/web-mirrors/lutterotti/luttero/laboratoriomateriali/Rietveld.pdf.
69 G. Will, *Powder diffraction: The Rietveld method and the two stage method to determine and refine crystal structures from powder diffraction data*, Springer-Verlag Berlin Heidelberg, 2006, pp. 44–69.
70 L. Lutterotti, M. Bortolotti, G. Ischia, I. Lonardelli and H. R. Wenk, *Z. Kristallogr., Suppl.*, 2007, **2007**, 125.
71 H. R. Wenk, L. Lutterotti and S. C. Vogel, *Powder Diffr.*, 2010, **25**, 283.
72 I. Lonardelli, H.-R. Wenk, L. Lutterotti and M. Goodwin, *J. Synchrotron Radiat.*, 2005, **12**, 354.
73 http://www.crystalimpact.com/diamond/download.htm.
74 A. Senyshyn, M. Hoelzel, T. Hansen, L. Vasylechko, V. Mikhailik, H. Kraus and H. Ehrenberg, *J. Appl. Crystallogr.*, 2011, **44**, 319.
75 http://polyhedra.org/poly/show/0/tetrahedron.
76 http://en.wikipedia.org/wiki/Deltahedron.
77 M. Crane, R. L. Frost, P. A. Williams and J. T. Kloprogge, *J. Raman Spectrosc.*, 2002, **33**, 62.
78 D. L. Rousseau, R. P. Bauman and S. P. S. Porto, *J. Raman Spectrosc.*, 1981, **10**, 253.
79 D. Christofilos, G. A. Kourouklis and S. Ves, *J. Phys. Chem. Solids*, 1995, **56**, 1125.
80 S. P. S. Porto and J. F. Scott, *Phys. Rev.*, 1967, **157**, 716.
81 M. Nicol and J. F. Durana, *J. Chem. Phys.*, 1971, **54**, 1436.
82 T. T. Basiev, A. A. Sobol, Y. K. Voronko and P. G. Zverev, *Opt. Mater.*, 2000, **15**, 205.
83 T. T. Basiev, A. A. Sobol, P. G. Zverev, L. I. Ivleva, V. V. Osiko and R. C. Powell, *Opt. Mater.*, 1999, **11**, 307.
84 A. Golubovic, R. Gajic, Z. Dohcevic-Mitrovic and S. Nikolic, *J. Alloys Compd.*, 2006, **415**, 16.
85 Y. Su, G. Li, Y. Xue and L. Li, *J. Phys. Chem. C*, 2007, **111**, 6684.
86 A. P. A. Marques, F. V. Motta, E. R. Leite, P. S. Pizani, J. A. Varela, E. Longo and D. M. A. de Melo, *J. Appl. Phys.*, 2008, **104**, 043505.
87 J. C. Sczancoski, M. D. R. Bomio, L. S. Cavalcante, M. R. Joya, P. S. Pizani, J. A. Varela, E. Longo, M. S. Li and J. A. Andrés, *J. Phys. Chem. C*, 2009, **113**, 5812.
88 D. Christofilos, S. Ves and G. A. Kourouklis, *Phys. Status Solidi B*, 1996, **198**, 539.
89 A. S. Barker Jr., *Phys. Rev.*, 1964, **135**, A742–A747.
90 Z. C. Ling, H. R. Xia, D. G. Ran, F. Q. Liu, S. Q. Sun, J. D. Fan, H. J. Zhang, J. Y. Wang and L. L. Yu, *Chem. Phys. Lett.*, 2006, **426**, 85.
91 R. K. Khanna and E. R. Lippincott, *Spectrochim. Acta*, 1968, **21A**, 905.
92 T. Thongtem, S. Kungwankunakorn, B. Kuntalue, A. Phuruangrat and S. Thongtem, *J. Alloys Compd.*, 2010, **506**, 475.
93 A. Golubovic, R. Gajic, Z. Dohcevic-Mitrovic and S. Nikolic, *Sci. Sintering*, 2006, **38**, 265.
94 P. Y. Jia, X. M. Liu, G. Z. Li, M. Yu, J. Fang and J. Lin, *Nanotechnology*, 2006, **17**, 734.
95 W. S. Wang, L. Zhen, C. Y. Xu, L. Yang and W. Z. Shao, *J. Phys. Chem. C*, 2008, **112**, 19390.
96 A. Phuruangrat, T. Thongtem and S. Thongtem, *J. Ceram. Soc. Jpn.*, 2008, **116**, 605.
97 B. T. Ahn, H. Jeon, B. Y. Hur, K. Kim and J. W. Park, *Solid State Phenom*, 2008, **124**, 315.
98 X.-Z. Li, B. Walker and A. Michaelides, *Proc. Natl. Acad. Sci. U. S. A.*, 2011, **108**, 6369.
99 R. Parthasarathi, V. Subramanian and N. Sathyamurthy, *J. Phys. Chem. A*, 2006, **110**, 3349.
100 J. Emsley, *Chem. Soc. Rev.*, 1980, **9**, 91.
101 A. W. Omta, M. F. Kropman, S. Woutersen and H. J. Bakker, *Science*, 2003, **301**, 347.
102 R. A. Klein, *J. Comput. Chem.*, 2002, **23**, 585.
103 L. Dougana, G. Z. Genchev, H. Lu and J. M. Fernandez, *Proc. Natl. Acad. Sci. U. S. A.*, 2011, **108**, 6369.
104 E. Zorebski, M. Piotrowska and M. Dzida, *Act. Phys. Polonica A*, 2008, **114**, A265.
105 http://www2.panasonic.com/consumer-electronics/shop/Home-Appliances/.
106 G. J. Wilson, A. S. Matijasevich, D. R. G. Mitchell, J. C. Schulz and G. D. Will, *Langmuir*, 2006, **22**, 2016.
107 Q. Yu, H. Lei, G. Yu, X. Feng, Z. Li and Z. Wu, *Chem. Eng. J.*, 2009, **155**, 88.
108 Y. Tian, B. Chen, H. Yu, R. Hu, X. Li, J. Sun, L. Cheng, H. Zhong, J. Zhang, Y. Zheng, T. Yu and L. Huang, *J. Colloid Interface Sci.*, 2011, **360**, 586.
109 P. Kubelka and F. Munk-Aussig, *Zeit. Für. Tech. Physik*, 1931, **12**, 593.
110 A. E. Morales, E. S. Mora and U. Pal, *Rev. Mex. Fis. S*, 2007, **53**, 18–22.
111 R. A. Smith. *Semiconductors*, 2nd edition. Cambridge University Press, London, 1978 p. 434.
112 R. Lacomba-Perales, J. Ruiz-Fuertes, D. Errandonea, D. Martínez-García and A. Segura, *Europhys. Lett.*, 2008, **83**, 37002.
113 M. Anicete-Santos, F. C. Picon, C. N. Alves, P. S. Pizani, J. A. Varela and E. Longo, *J. Phys. Chem. C*, 2011, **115**, 12180.
114 W. F. Zhang, Z. Yin and M. S. Zhang, *Appl. Phys. A: Mater. Sci. Process.*, 2000, **70**, 93.
115 W. F. Zhang, Z. Yin and M. S. Zhang, *J. Phys.: Condens. Matter*, 1999, **11**, 5655.
116 G. Blasse and M. Wiegel, *J. Alloys Compd.*, 1995, **224**, 342.
117 M. V. Korzhik, V. B. Pavlenko, T. N. Timoschenko, V. A. Katchanov, A. V. Singovskii, A. N. Annenkov, V. A. Ligun, I. M. Solskii and J. P. Peigneux, *Phys. Status Solidi A*, 1996, **154**, 779.
118 E. V. Sokolenko, V. M. Zhukovskii, E. S. Buyanova and Y. A. Krasnobaev, *Inorg. Mater*, 1998, **34**, 499.
119 B. M. Sinelnikov, E. V. Sokolenko and V. Y. Zvekov, *Inorg. Mater*, 1996, **32**, 999.
120 D. Chen, G. Z. Shen, K. B. Tang, H. G. Zheng and Y. T. Qian, *Mater. Res. Bull.*, 2003, **38**, 1783.
121 Y. T. Chen, J. Li, X. T. Chen, J. M. Hong, Z. L. Xue and X. Z. You, *J. Cryst. Growth*, 2003, **253**, 361.
122 R. Zhai, H. Wang, H. Yan and M. Yoshimura, *J. Cryst. Growth*, 2006, **289**, 647.
123 Z. L. Wang, G. Z. Li, Z. W. Quan, D. Y. Kong, X. M. Liu, M. Yu and J. Lin, *J. Nanosci. Nanotechnol*, 2007, **7**, 602.

124 T. Y. Liu, J. Chen and F. N. Yan, *J. Lumin.*, 2009, **129**, 101.
125 C. Y. Pu, T. Y. Liu and Q. R. Zhang, *Phys. Status Solidi B*, 2008, **245**, 1586.
126 E. Longo, E. Orhan, F. M. Pontes, C. D. Pinheiro, E. R. Leite, J. A. Varela, P. S. Pizani, T. M. Boschi, F. Lanciotti, A. Beltrán and J. Andrés, *Phys. Rev. B: Condens. Matter Mater. Phys.*, 2004, **69**, 125115.
127 V. M. Longo, E. Orhan, L. S. Cavalcante, S. L. Porto, J. W. M. Espinosa, J. A. Varela and E. Longo, *Chem. Phys.*, 2007, **334**, 180.
128 L. S. Cavalcante, J. C. Sczancoski, R. L. Tranquilin, J. A. Varela, E. Longo and M. O. Orlandi, *Particuology*, 2009, **7**, 353.
129 K. P. F. Siqueira, M. L. Moreira, M. Valadares and A. Dias, *J. Mater. Sci.*, 2010, **45**, 6083.
130 L. Gracia, V. M. Longo, L. S. Cavalcante, A. Beltrán, W. Avansi, M. S. Li, V. R. Mastelaro, J. A. Varela, E. Longo and J. Andrés, *J. Appl. Phys.*, 2011, **110**, 043501.
131 Z. Ju, R. Wei, X. Gao, W. Liu and C. Pang, *Opt. Mater.*, 2011, **33**, 909.
132 J. Liao, B. Qiu, H. Wen and W. You, *Opt. Mater.*, 2009, **31**, 1513.

Downloaded by UNIVERSIDAD SAO PAULO on 07 February 2012
Published on 18 November 2011 on http://pubs.rsc.org | doi:10.1039/C1CE05977G

 This journal is © The Royal Society of Chemistry 2012